2

Device Simulation

M. Schröter[1,2], G. Wedel[1], N. Rinaldi[3] and C. Jungemann[4]

[1]Chair for Electron Devices and Integrated Circuits, Technische Universität Dresden, Germany
[2]Department of Electrical and Computer Engineering, University of California at San Diego, USA
[3]Department of Electrical Engineering and Information Technology, University Federico II, Italy
[4]RWTH Aachen University, Germany

2.1 Numerical Simulation

G. Wedel and M. Schröter

Numerical simulation (including TCAD) tools were heavily used during DOTSEVEN, aiding the device design and optimization during process development and the physical understanding of the HBT operation so as to support compact modeling. In addition, based on earlier work during DOTFIVE on exploring the physical limitations of SiGe HBTs [Sch11], various numerical simulation tools were used to create the first comprehensive and detailed roadmap in cooperation with the radio-frequency/analog mixed-signal committee of the International Technology Roadmap of Semiconductors (ITRS)[1] consortium in 2014. The flowchart displayed in Figure 2.1 for finding the vertical and lateral HBT structure of a major ITRS technology node is an example for the large variety of simulation tools that were

[1]In the course of the semiconductor industry consolidation only very few companies have remained that have the financial means for developing advanced CMOS technologies. Pursuing partially diverse manufacturing approaches for the associated MOSFET structures, the common basis for technology development, which initially led to the ITRS consortium, is gradually disappearing and rather results in a competition. Hence, the ITRS consortium has been abandoned by the CMOS industry in 2015. The performance tables of the ITRS have been taken over by the IRDS consortium.

developed and employed in DOTFIVE and in DOTSEVEN, since the same approach has been used to define the DOTSEVEN target HBT structure. As already mentioned in-house tools for carrier transport have been based on the DD, HD and BTE approach. In particular, a new deterministic BTE solver was developed and applied to SiGe HBTs, which is described in Section 2.2.2 In addition, simulation tools were developed for the analysis of thermal and parasitic effects in advanced HBTs.

A three-dimensional (3D) thermal solver was used for investigating the temperature distribution within the device structure and its impact on the HF characteristics. A more detailed analysis was performed and insights into the microscopic effects of self-heating were gained with a new Boltzmann solver for phonon transport which was then coupled to the already existing spherical harmonics expansion based BTE solver for charge carrier transport. This approach, which allows deeper insights into device reliability, is described in Section 2.3.

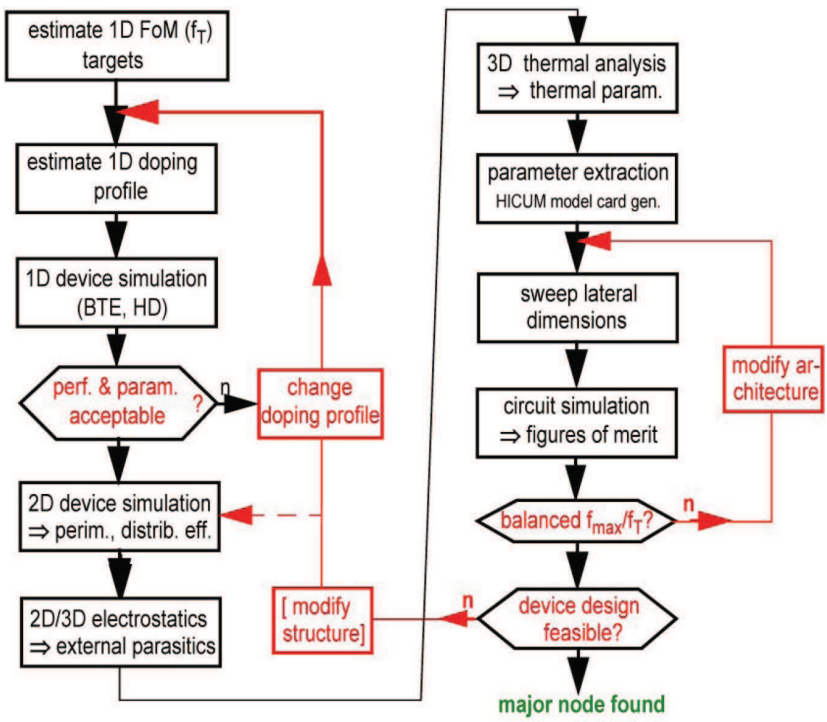

Figure 2.1 Flowchart for finding the vertical and lateral HBT structure of a major technology node [Sch17].

In order to obtain a realistic estimate for the HF device performance, a 3D Poisson solver has been used to calculate the various parasitic capacitances within an actual 3D transistor structure.

2.2 Device Simulation

2.2.1 TCAD Device Optimization

The device design of advanced SiGe HBTs demands an as accurate as possible prediction of the electrical behavior in order to shorten the time from process development of new devices to product and to identify promising device structures during the early stage of process development. Therefore, technology computer aided design (TCAD) software offers a relatively fast and cost effective approach, compared to fabricating and measuring test devices. Of course, the predictive capability of TCAD strongly depends on the accuracy of the employed physical models, such as those for carrier transport, and their parameters.

The most widely used description for carrier transport is the so called drift-diffusion (DD) model, which has been the workhorse in industry for over 40 years. The DD transport model is derived from the Boltzmann transport equation (BTE) by taking the first moments [Jun03][Sel84][Lun00] and consists of the

- Poisson equation,
- hole and electron continuity equation and
- carrier transport equations.

Its major advantage is the low computational cost in terms of both memory requirements and simulation time. However, these advantages are obtained at the cost of physical accuracy, especially for today's SiGe HBTs. For example, the DD transport model significantly underestimates the HF performance of advanced SiGe HBTs (i.e. too low transit frequencies f_T) and overestimates the impact of the Avalanche effect (e.g. too low BVCEO).

For improving the accuracy while maintaining reasonable simulation times, the hydrodynamic (HD) and the energy transport (ET) model were introduced. These models can also be derived from the BTE [Jun03][Lun00] and include a description of energy transport. The ET model neglects the momentum conservation and is thus a subset of HD model. The latter consists of the

- Poisson equation,
- hole and electron continuity equation,

- hole and electron transport equations,
- hole and electron energy balance equations and
- hole and electron energy flux equations.

Compared to DD, the HD transport model considers two additional equations for each carrier type. In addition and due to the two additional equations, new physical quantities, like the carrier energy relaxation time (for the energy balance equation) and the thermal conductivity involved in the energy flux description are introduced. Another point in terms of the HD transport model is the impact of the carrier temperature (solution variable of the energy balance equation as a representation of the kinetic carrier energy) on the carrier transport equation. For the transport equation, the impact of the carrier temperature, especially its gradient acting as additional driving force, needs to be rather heuristically adjusted than set by physics-based considerations in order to obtain reasonable results w.r.t. measurements or BTE simulation data [Wed10]. Once the above mentioned issues have been clarified, a reasonable agreement between HD and BTE can be obtained in terms of terminal characteristics, like transfer currents or transit frequencies. In addition, the HD simulation times are only slightly longer (by a factor of 1.5 up to 3.5) than those of DD simulation. However, BTE results or, if available, measurement data are needed for adjusting the HD transport model. Thus for the design of advanced devices and realistic estimations of their performance, a BTE solver is inevitable.

For solving the BTE, two kinds of methods exist: stochastic solvers based on the Monte-Carlo (MC) method [Jun03][Tom93][Jac83] and deterministic solvers [Hon11][Gal05][Wed16], which solve the BTE directly based on discretized equations just like in the DD and HD case. The MC method is more widely used, since it offers a relatively low implementation effort. In addition, the memory consumption is low compared to deterministic solvers. However, the major drawbacks of the MC method are long simulation times (since MC is inherently a transient method), noisy results (due to its stochastic nature) and a insufficient resolution of minority carrier densities, e.g. electrons in the base region of an HBT. These drawbacks and the advances in computer performance (faster CPUs and cheaper memory) gave rise to the development of deterministic solvers. These solvers enable the calculation of stationary solutions, which are smooth and noise free even for minority carriers. However, these advantages are obtained at the cost of a high memory consumption and especially a much more elaborate mathematical preprocessing and implementation effort. Despite the strong reduction in simulation time compared to the MC method, the computational effort still is significantly

higher compared to DD and HD. Thus, the use of even deterministic BTE solvers is practically not feasible for direct device design optimization, but remains restricted to the 1D carrier transport and serves mostly as a reference solution for advanced vertical HBT structures.

2.2.2 Deterministic BTE Solvers

The BTE is a seven-dimensional integro-differential equation defined over the three real space dimensions (*x,y,z*), the three dimensions over the reciprocal space (k_x, k_y, k_z) and time *t*. In conservative form, the BTE for electrons reads [Jun03][Lun00][Honll][Gal05][Wedl6]

$$\frac{\partial f^v}{\partial t} + \nabla_{\vec{r}} \bullet (\vec{v}_g^{\,v} f^v) - \frac{q}{\hbar} \nabla_{k\vec{v}} \bullet (\vec{E}_{\text{eff}}^{\,v} f^v) = C, \tag{2.1}$$

with the particle distribution function (PDF) f^v as the solution variable of the BTE (with $0 < f^v \leq 1$), the carrier group velocity $\vec{v}_g^{\,v}$ and the collision term *C*. The effective field $\vec{E}_{\text{eff}}^{\,v}$ is defined as [Hon11][Wed16]

$$\vec{E}_{\text{eff}}^{\,v} = \nabla_{\vec{r}} \left(-\psi + \frac{E_{\text{C},0}^v}{q} + \frac{\varepsilon^v}{q} \right) \tag{2.2}$$

with the electrostatic potential ψ obtained by the Poisson equation, the material/composition dependent band edge $E_{\text{C},0}^v$ and the kinetic energy ε^v. The variable *v* denotes the observed valley within the first Brillouin-zone of the reciprocal space. For the sake of readability, the dependencies of the quantities involved have been omitted and are here shortly summarized:

- f^v is a function of $\vec{r}$, $\vec{k}^v$ and time *t*;
- $\vec{v}_g^{\,v}$ is a function of $\vec{r}$ and $\vec{k}^v$;
- ψ is a function of $\vec{r}$ and time *t*;
- $E_{\text{C},0}^v$ is a function of $\vec{r}$;
- ε^v is a function of $\vec{r}$ and $\vec{k}^v$.

The collision term *C* describes the carrier interaction (scattering) due to lattice vibrations (phonon scattering), impurities/alloys and other carriers.

For each considered scattering mechanism, a transition rate S^{X} (X is a placeholder for the considered scattering mechanism) is obtained by Fermi's Golden Rule and the collision term becomes (see e.g. [Jun03][Lun00])

$$C = \sum_{\text{X}} \sum_{\vec{k}^{v'}} S^{\text{X}}(\vec{k}^{v'} \rightarrow \vec{k}^{v}) f^{v'}(1 - f^{v}) - S^{\text{X}}(\vec{k}^{v} \rightarrow \vec{k}^{v'}) f^{v}(1 - f^{v'}), \tag{2.3}$$

where the summation over $\overrightarrow{k}^{v'}$ discards the spin degeneracy [Lun00]. The first term within the sums describes the in-scattering and the second one the out-scattering of particles, respectively. Equation (2.3) sums first over all possible $\overrightarrow{k}^{v'}$ (defined by the transition rate (S^{X})) from where in- or out-scattering might occur and sums these results up for each scattering mechanism. The formulation of the collision term (2.3) contains terms $(1-f^{v,v'})$, which measures the vacancy of the state $\overrightarrow{k}^{v/v'}$, respectively. Thus, in- or out-scattering might be blocked due to a fully occupied state, which is called Pauli-exclusion principle [Hon11]. For low doping concentrations, where the Fermi-level is sufficiently far away from the conduction band edge (non-degenerate semiconductor), the PDFs $f^{v,v'}$ are much smaller than one. In this case, (2.3) can be simplified to

$$C \cong \sum_{\mathrm{X}} \sum_{\overrightarrow{k}^{v'}} S^{\mathrm{X}}(\overrightarrow{k}^{v'} \rightarrow \overrightarrow{k}^{v}) f^{v'} - S^{\mathrm{X}}(\overrightarrow{k}^{v} \rightarrow \overrightarrow{k}^{v'}) f^{v}. \tag{2.4}$$

However, in both Equations (2.3) and (2.4) it is summed over discrete final states $\overrightarrow{k}^{v'}$. Under the assumption that adjacent states are close enough, these states are assumed to be continuous and the sum is converted into an integral by the relation [Gal05][Wed16]

$$\sum_{\overrightarrow{k}^{v'}} \cdots \rightarrow \frac{\Omega}{(2\pi)^3} \int \cdots d\overrightarrow{k}^{v'}, \tag{2.5}$$

with the crystal volume Ω. Thus, with (2.5) the collision terms become [Hon11][Gal05][Wed16]

$$C = \frac{\Omega}{(2\pi)^3} \sum_{\mathrm{X}} \int (S^{\mathrm{X}}(\overrightarrow{k}^{v'} \rightarrow \overrightarrow{k}^{v}) f^{v'}(1 - f^{v}) - S^{\mathrm{X}}(\overrightarrow{k}^{v} \rightarrow \overrightarrow{k}^{v'}) \\ f^{v}(1 - f^{v'}))d\overrightarrow{k}^{v'} \tag{2.6}$$

for the degenerate case and

$$C = \frac{\Omega}{(2\pi)^3} \sum_{\mathrm{X}} \int (S^{\mathrm{X}}(\overrightarrow{k}^{v'} \rightarrow \overrightarrow{k}^{v}) f^{v'} - S^{\mathrm{X}}(\overrightarrow{k}^{v} \rightarrow \overrightarrow{k}^{v'}) f^{v}) d\overrightarrow{k}^{v'} \tag{2.7}$$

for the non-degenerate case.

Thus, the considered system of equations is set up by the BTE (2.1) with the effective field (2.2) and the collision terms (2.6) or (2.7). For the numerical treatment, it is more advantageous to express the vectors $\overrightarrow{k}^{v}$ and $\overrightarrow{k}^{v'}$ in terms of the kinetic energy ε^{v} and $\varepsilon^{v'}$, measured from the minimum of the valley v/v', respectively. For carrier scattering, both momentum and energy conservation has to be fulfilled (see e.g. [Lun00]). However, due to the complex shape of the phonon energy as function of the scattering vector $\overrightarrow{\beta} = \overrightarrow{k}^{v'} - \overrightarrow{k}^{v}$ and the demand of $\varepsilon^{v'}(\overrightarrow{k}^{v'}) = \varepsilon^{v}(\overrightarrow{k}^{v}) \pm \hbar\omega(\overrightarrow{\beta}) + (E^{v}_{\mathrm{C},0} - E^{v'}_{\mathrm{C},0})$ (energy conservation), approximations are employed for the phonon energy as function of the scattering vector, which relax the momentum conservation. In practice, modeling the scattering is mainly focused on the energy conservation, since $\hbar\omega(\overrightarrow{\beta})$ is approximated to be either zero (elastic scattering) or constant (inelastic scattering). With these simplifications, it is equivalent to consider the kinetic energies. Thus for the BTE, a coordinate transformation has to be performed and the valley dispersion relation $\varepsilon^{v}(\overrightarrow{k}^{v})$ needs to be a analytic and invertible function. The most commonly used dispersion relation is the non-parabolic one [Lun00][Tom93][Hon11][Gal05][Wed16]

$$\varepsilon v(1+\alpha\varepsilon^{v}) = \frac{\hbar^2}{2m_0 m^*}|\overrightarrow{k}^{v}|^2, \tag{2.8}$$

with the effective mass m^* and the non-parabolicity factor α. This dispersion relation models equi-energy surfaces in the reciprocal space as spheres (due to $|\overrightarrow{k}^{v}|^2$), where α describes the increase of energy for increasing $|\overrightarrow{k}^{v}|$. For $\alpha = 0$, a parabolic dispersion relation is obtained, where the kinetic energy increases quadratically with $|\overrightarrow{k}^{v}|$. With (2.8), the vector $\overrightarrow{k}^{v}$ can be expressed in spherical coordinates [Hon11][Gal05][Wed16]

$$\overrightarrow{k}^{v} = \frac{\sqrt{2m_0 m^*}}{\hbar}\sqrt{\varepsilon^{v}(1+\alpha\varepsilon^{v})}\begin{bmatrix} \mu \\ \sqrt{1-\mu^2}\cos(\varphi) \\ \sqrt{1-\mu^2}\sin(\varphi) \end{bmatrix}, \tag{2.9}$$

with μ as the cosine of the polar angle and the azimuthal angle φ. In (2.9), the spherical coordinate system is rotated to measure the polar angle μ w.r.t. the k^{v}_{x}-axis instead of the k^{v}_{z}-axis. This rotation is advantageous for 1D simulations in x-direction, since it allows to omit φ due to the rotational symmetry of the PDF. Thus in this case, only two dimensions (ε^{v} and μ) have to be discretized instead of the full $[k_x k_y k_z]$ space [Honll][Wedl6].

Nevertheless, the equi-energy surfaces do usually not exhibit a spherical shape within the first Brillouin-zone of the reciprocal space. For example in Si, ellipsoids aligned to the axis $[k_x k_y k_z]$ are found for the so called X-valleys, which mainly contribute to the carrier transport. Thus, the dispersion relation (2.8) becomes in this case

$$\varepsilon^v(1+\alpha\varepsilon^v) = \frac{\hbar}{2m_0}\left(\frac{(k_x^v)^2}{m_x^v} + \frac{(k_y^v)^2}{m_y^v} + \frac{(k_z^v)^2}{m_z^v}\right), \tag{2.10}$$

with the anisotropic effective masses m_x^v, m_y^v and m_z^v. In order to account for the valley anisotropy in (2.9), the Herring-Vogt transformation [Her56] is employed, which basically scales the axis $[k_x^v\ k_y^v\ k_z^v]$ in such a way that the ellipsoids are mapped to spheres. After the mapping, the considered *k*-space $[\widetilde{k}_x^v\ \widetilde{k}_y^v\ \widetilde{k}_z^v]$ is given by

$$\vec{\widetilde{k}}^v = [T^{\mathrm{HV},v}] \bullet \vec{k}^v, \tag{2.11}$$

$$\vec{\widetilde{k}}^{\,v} = \frac{\sqrt{2m_0 m_v^*}}{\hbar}\sqrt{\varepsilon^v(1+\alpha\varepsilon^v)}\begin{bmatrix} \mu \\ \sqrt{1-\mu^2}\cos(\varphi) \\ \sqrt{1-\mu^2}\sin(\varphi) \end{bmatrix}, \tag{2.12}$$

with the Herring-Vogt transformation matrix

$$[T^{\mathrm{HV},v}] = \begin{bmatrix} \sqrt{\frac{m_v^*}{m_x^v}} & 0 & 0 \\ 0 & \sqrt{\frac{m_v^*}{m_y^v}} & 0 \\ 0 & 0 & \sqrt{\frac{m_v^*}{m_z^v}} \end{bmatrix}, \tag{2.13}$$

and the effective mass $m_v^* = \sqrt[3]{m_x^v m_y^v m_z^v}$. Like for the isotropic dispersion relation (2.8) and its *k*-vectors (2.9), also for the anisotropic description (2.10) and the *k*-vectors (2.11)–(2.12), the φ-dependence can be omitted for 1D simulations in *x*-direction, as long as the Herring-Vogt matrix does not contain off-diagonal elements. This assumption holds for the X-valleys in Si/SiGe, but not for the L-valleys in some III–V materials, like GaAs. If one considers the 1D transport in *x*-direction, the effective field $\vec{E}_{\mathrm{eff}}^{\,v}$ consists only of a non-zero *x*-component. Thus, the PDF is only altered by the effective field in k_x^v-direction. If the equi-energy surfaces are spheres or ellipsoids, aligned to the $[k_x k_y k_z]$ axis, their rotational symmetry allow to omit φ. Otherwise, a change of the PDF in k_x^v-direction forces changes in the $\widetilde{k}_x^v$, $\widetilde{k}_y^v$

and $\widetilde{k}_z^v$ directions and the PDF does not exhibit a rotational symmetry on the equi-energy surfaces anymore. Focusing on Si/SiGe and considering the x-direction only, the BTE (1) simplifies to [Wed16]

$$\frac{\partial f^v}{\partial t} + \frac{d}{dx}(T_{1,1}^{\mathrm{HV},v}\widetilde{v}_g^{v,x} f^v) - \frac{q}{\hbar}\nabla_{\overrightarrow{\tilde{k}^v}} \bullet (T^{\mathrm{HV},v} \bullet \overrightarrow{E}_{\mathrm{eff}}^v f^v) = C, \tag{2.14}$$

with the carrier group-velocity

$$\widetilde{v}_g^{v,x} = \frac{1}{\hbar}\frac{\partial}{\partial \widetilde{k}_x^v}\varepsilon^v\left(\overrightarrow{\tilde{k}^v}\right) \tag{2.15}$$

after the Herring-Vogt transformation and $T_{1,1}^{\mathrm{HV},v}$ being the first main-diagonal element of the matrix (2.13). Assuming a spatial independent transformation matrix $T^{\mathrm{HV},v}$, the BTE (2.14) transforms into the ε^v/μ-space to

$$\frac{\partial f^v}{\partial t} + \frac{d}{dx}(a_x f^v) - \frac{q}{\hbar \mathrm{dos}^v(\varepsilon^v)}\left\{\frac{\partial}{\partial \varepsilon^v}(a_{\varepsilon^v} f^v) + \frac{\partial}{\partial \mu}(a_\mu f^v)\right\} = C \tag{2.16}$$

with the flux coefficients

$$a_x = \frac{1}{\hbar}\frac{\mu T_{1,1}^{\mathrm{HV},v}}{\frac{\mathrm{d}}{\mathrm{d}\varepsilon^{\mathrm{v}}}|\overrightarrow{\tilde{k}^v}|}, \tag{2.17}$$

$$a_{\varepsilon^v} = \frac{\mu \mathrm{dos}^v(\varepsilon^v)}{\frac{\mathrm{d}}{\mathrm{d}\varepsilon^{\mathrm{v}}}|\overrightarrow{\tilde{k}^v}|} T_{1,1}^{\mathrm{HV},v}, E_{\mathrm{eff}}^{v,x}, \tag{2.18}$$

$$a_{\mu^v} = \frac{(1-\mu^2)\mathrm{dos}^v(\varepsilon^v)}{|\overrightarrow{\tilde{k}^v}|} T_{1,1}^{\mathrm{HV},v}, E_{\mathrm{eff}}^{v,x}, \tag{2.19}$$

the abbreviation

$$\frac{\mathrm{d}}{\mathrm{d}\varepsilon^{\mathrm{v}}}|\tilde{k^v}| = \frac{\sqrt{2m_0 m_v^*}}{\hbar}\frac{1}{2}\frac{1+2\alpha\varepsilon^v}{\sqrt{\varepsilon^v(1+\alpha\varepsilon^v)}} \tag{2.20}$$

and the density of states

$$\mathrm{dos}^v(\varepsilon^v) = \frac{1}{2}\left(\frac{\sqrt{2m_0 m_v^*}}{\hbar}\right)^3 \sqrt{\varepsilon^v(1+\alpha\varepsilon^v)}(1+2\alpha\varepsilon^v), \tag{2.21}$$

which can be viewed as the transformed infinitesimal volume element

$$\overrightarrow{d\tilde{k}^v} = \mathrm{dos}^v(\varepsilon^v) d\varepsilon^v d\mu d\varphi. \tag{2.22}$$

At this point, the analytic pre-considerations/pre-processing, necessary for the discretization, is almost done. There are various approaches, such as the spherical harmonics expansion (SHE) [Hon11] or BIM-WENO approach [Gal05][Wed16], which rely on the same underlying equations but differ in the numerical representation for f^v (PDF). The choice of the ansatz for f^v strongly affects the further treatment of the collision term. However, regardless of the SHE or BIM-WENO ansatz, the transformed BTE (2.16) is multiplied by the density of states (2.21) and integrated over a discretized control volume in the reciprocal space. After the numerical representation of the derivatives and integrals (collision term) involved, a set of equations (for each discretization point) is obtained, which finally results in a sparse matrix to be solved. The system to be solved also contains the Poisson equation, needed for the electrostatic potential involved in the effective field $\overrightarrow{E}^v_{\text{eff}}$ (2.2). The main burden of solving the BTE deterministically arises from the number of needed discretization points, especially for ε^v. The step size for ε^v has to be fine enough to capture all energy exchanges by phonons, since otherwise these scattering processes get smeared out by others and results in less accurate results.

2.2.3 Drift-diffusion and Hydrodynamic Transport Models

As mentioned at the beginning of this chapter, both the DD and the HD transport model can be derived from the BTE by the method of moments with some simplifications. The Poisson and the continuity equations are employed in both DD and HD analysis. The Poisson equation reads

$$\nabla_{\vec{r}} \cdot (\varepsilon_0 \varepsilon_r \nabla_{\vec{r}}(\psi)) = -q(p - n + N_{\text{D}} - N_{\text{A}}), \tag{2.23}$$

with the relative material permittivity ε_r, the elementary charge *q,* and the donor and acceptor doping concentration N_{D} and N_{A}, respectively. The carrier continuity equation reads

$$\nabla_{\vec{r}} \cdot (\overrightarrow{J}_c) = -\text{sgn}(c) q \left(R + \frac{\partial c}{\partial t} \right) \tag{2.24}$$

with the carrier density *c,* the carrier current density $\overrightarrow{J}_c$ and the net recombination rate *R*.

The first difference between the DD and HD transport models is found for the carrier transport equation [Syn15]

$$\begin{aligned} \overrightarrow{J}_c = {} & qc\mu_c \overrightarrow{E}_{c,\text{eff}} - q\text{sgn}(c)\mu_c V_{\text{T},c} \nabla_{\vec{r}} c \\ & - \text{sgn}(c)\mu_c c k_{\text{B}} \left[f^{\text{td}} + \log\left(\frac{N_{\text{X}}}{n_{\text{ir}}} \right) \right] \nabla_{\vec{r}} T_c \end{aligned} \tag{2.25}$$

where the first two terms on the r.h.s. of (2.25) represent drift and diffusion transport, and the last term considers the gradient of the carrier temperature T_c acting as additional driving force for the carrier transport process. Here, μ_c is the carrier mobility, $V_{\mathrm{T},c}$ is the thermal voltage for the carrier temperature T_c, N_x is the effective density of states of electrons and holes (depending on c), n_{ir} is the reference intrinsic carrier density, and f^{td} is a HD transport model parameter. Finally, $\overrightarrow{E}_{c,\mathrm{eff}}$ is the effective field given by

$$\overrightarrow{E}_{c,\mathrm{eff}} = -\nabla_{\overrightarrow{r}}(\Psi - \mathrm{sgn}(c)V_{\mathrm{B,c}}) \tag{2.26}$$

with the carrier band potential $V_{\mathrm{B,c}}$ accounting for the impact of high-doping and material composition effects on the respective band edge. Equations (2.24)–(2.26) contain the function sgn, which is depends the carrier type:

$$\mathrm{sgn}(c) = \left\{ \begin{matrix} -1, \text{ for electrons (c = n)}, \\ 1, \text{ for holes (c = p)}. \end{matrix} \right\}. \tag{2.27}$$

The DD transport model consists of Equations (2.23)–(2.26), with a carrier temperature equal to the lattice temperature ($T_{\mathrm{c}} = T_{\mathrm{L}}$). Thus, for isothermal DD simulations, the last term on the r.h.s. in (2.25) vanishes. In the case of HD simulations, the carrier temperature T_{c} is obtained by the energy balance equation

$$\frac{\partial}{\partial t} c\omega_c = \overrightarrow{J}_c \cdot \overrightarrow{E}_{c,\mathrm{eff}} - (\nabla_{\overrightarrow{r}} \cdot \overrightarrow{S}_c) - R\omega_c + c\frac{\partial \omega_c}{\partial t}\bigg|_{\mathrm{coll.}}, \tag{2.28}$$

with $\omega_c = \frac{3}{2} k_{\mathrm{B}} T_C$ and the energy flux

$$\overrightarrow{S}_c = -\left(\frac{5}{2} + f^{\mathrm{tc}}\right)\left(\frac{k_{\mathrm{B}}}{q}\right)^2 qc\mu_c \nabla_{\overrightarrow{r}} T_c + \mathrm{sgn}(c)\left(\frac{5}{2} + f^{\mathrm{ec}}\right)\frac{k_{\mathrm{B}} T_c}{q}\overrightarrow{J}_c. \tag{2.29}$$

Here, the first term on the r.h.s. Represents contains the thermal conductivity after Wiedemann-Franz and the gradient of the carrier temperature (energy transport due to spatially different carrier temperatures), where the second term models the energy transport due to the carrier current density. Within (2.25) and (2.29), three parameters f^{td}, f^{tc} and f^{ec} are available in the HD case for adjusting the impact of the respective contributions. These parameters are usually not fixed and vary across technologies and generations in the same material [Wed10]. The parameters are usually obtained by adjusting the HD terminal behavior (such as transfer and output characteristics and transit

frequency) to those obtained by BTE simulations or, if available, to measured results. The simplicity of the DD and HD transport models demands an elaborate set of physical material models for the

- carrier mobility (low and high field case, DD, HD),
- recombination and generation (DD, HD),
- band potential (DD, HD), and
- energy relaxation time (HD only).

Usually, the material models are developed and their parameters are adjusted to BTE simulations of bulk material, where a homogenous and infinitely large semiconductor is assumed.

2.2.4 Simulation Examples

The intention of this section is to give an rough impression about the applicability of DD and HD transport models compared to the BTE for SiGe HBTs. As an example, a one-dimensional (1D) SiGe HBT structure with $f_{\mathrm{T}} \approx 630$ GHz [Paw09] is considered. The doping and Germanium profile is shown in Figure 2.2.

2.2.4.1 DD simulation

The DD transfer characteristic and the transit frequency for the considered device are shown in Figure 2.3 and compared with the results obtained by the deterministic BTE solver based on the spherical harmonics expansion (SHE) of the electron distribution function [Hon11].

Compared to the BTE results, a reasonable agreement for the transfer characteristic between DD transport and BTE is obtained up to the onset of collector high current effects. However, DD severely underestimates the

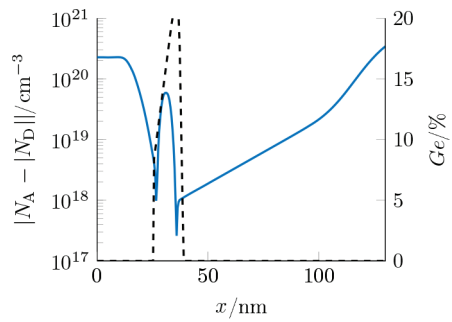

Figure 2.2 Net doping and Germanium profile of a SiGe HBT with f_{T} = 630 GHz.

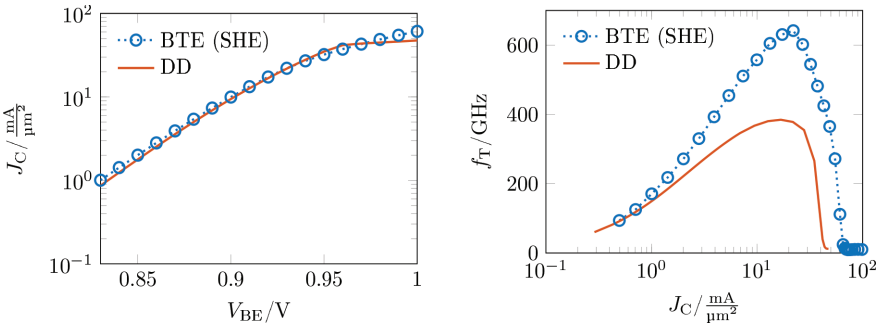

Figure 2.3 Transfer characteristic (left) and transit frequency (right) obtained from DD transport and BTE for the device of Figure 2.2. $V_{CE} = 1$ V.

transit frequency f_T. The main origin of the discrepancies is coming from the assumptions involved in the derivation of the DD transport model. For DD, it is assumed that the distribution function is in equilibrium with the lattice. Thus, any displacement of the distribution function (towards higher kinetic energies) is not directly taken into account, but indirectly by the electron velocity versus electric field model. Usually, a saturation drift velocity limits the carrier velocity although the velocity obtained by BTE might in some regions exceed that saturation limit (velocity overshoot) as shown in Figure 2.4(a) for the peak f_T range. Thus, DD predicts slower electrons and, for the same current, a higher electron density in the base-collector region (cf. Figure 2.4(b)). This results in a higher electron transit time and thus, compared to the BTE, a lower f_T. The constant DD electron density within

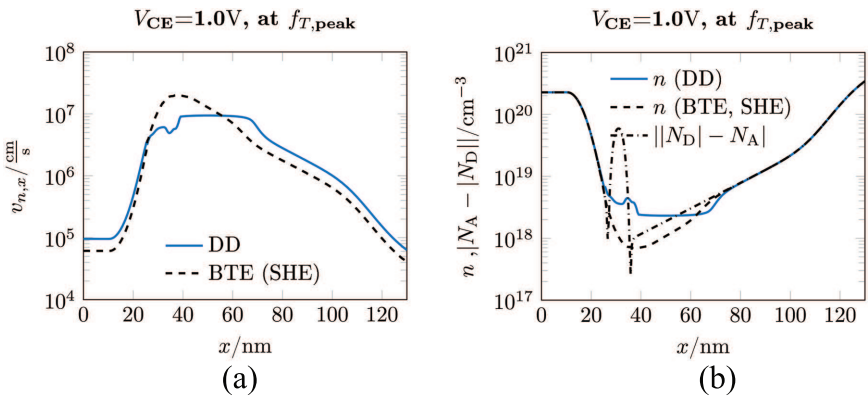

Figure 2.4 Electron velocity and density obtained by DD and BTE simulation.

the BC space charge region (SCR) is the result of the saturation drift velocity used in the DD simulation.

The discrepancies shown in Figures 2.3 and 2.4 are one example of the deficiency of DD transport models. Another one is the underestimation of the breakdown voltage.

2.2.4.2 HD simulation

Here, the most critical parameters are f^{td}, f^{tc} and f^{ec} introduced in Section 2.2.3. These parameters have a significant impact on the terminal characteristics, which can even show a non-physical behavior. Usually, a parameter constellations can be found that gives HD simulation results close to the ones obtained by the BTE. For the SiGe HBT in Figure 2.2, the impact of each of the above parameters is illustrated below. Figure 2.5 shows transfer, transit frequency and output characteristic for different values of f^{td}, while the remaining parameters are kept at zero.

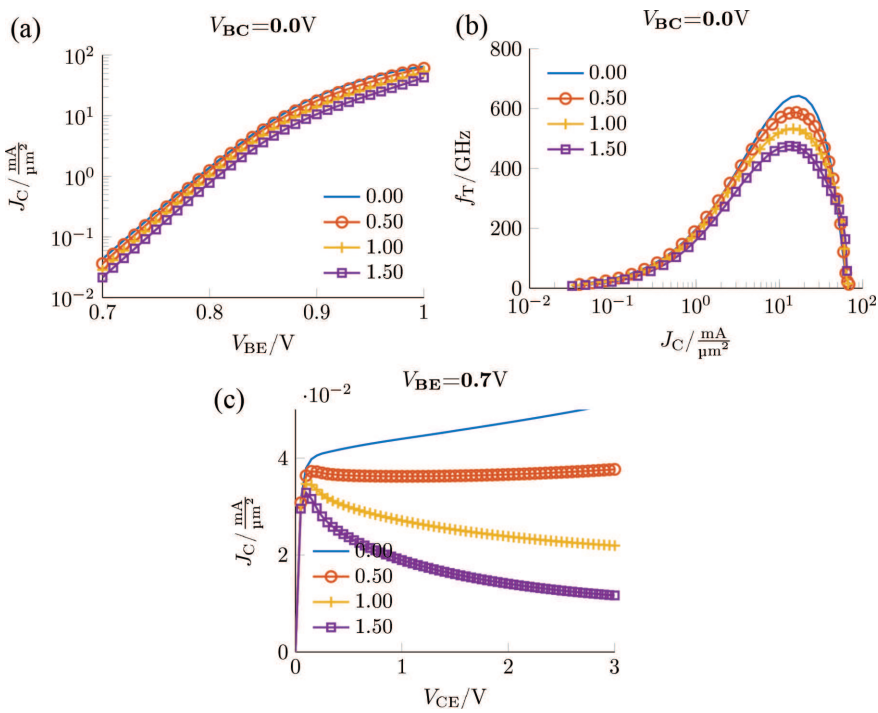

Figure 2.5 Illustration of the impact of f^{td} on the transfer characteristic, transit frequency and output characteristics for $f^{\mathrm{tc}} = f^{\mathrm{ec}} = 0$.

With increasing values of f^{td} both the collector current density and the transit frequency are decreasing, while the output conductance decreases and can even become negative and thus non-physical in this case (of constant V_{BE}). This is caused by a too strong gradient of the carrier temperature acting as driving force of the electron current. Thus, although f^{td} often requires larger values for adjusting $f_{\mathrm{T,peak}}$ it needs to be limited. Fortunately, with the parameter f^{tc} the impact of f^{td} on the output characteristics can be damped as shown in Figure 2.6. With f^{tc}, the thermal conductivity involved in the energy flux equation (2.29) is altered. The smaller f^{tc} the less energy is transported by the gradient of the carrier temperature. Thus, the carrier temperature profile becomes less smeared within the device, which in turn diminishes the impact of the carrier temperature gradient on the transport equation (2.25). With a increasing f^{tc}, the collector current densities are increased along with the output conductance.

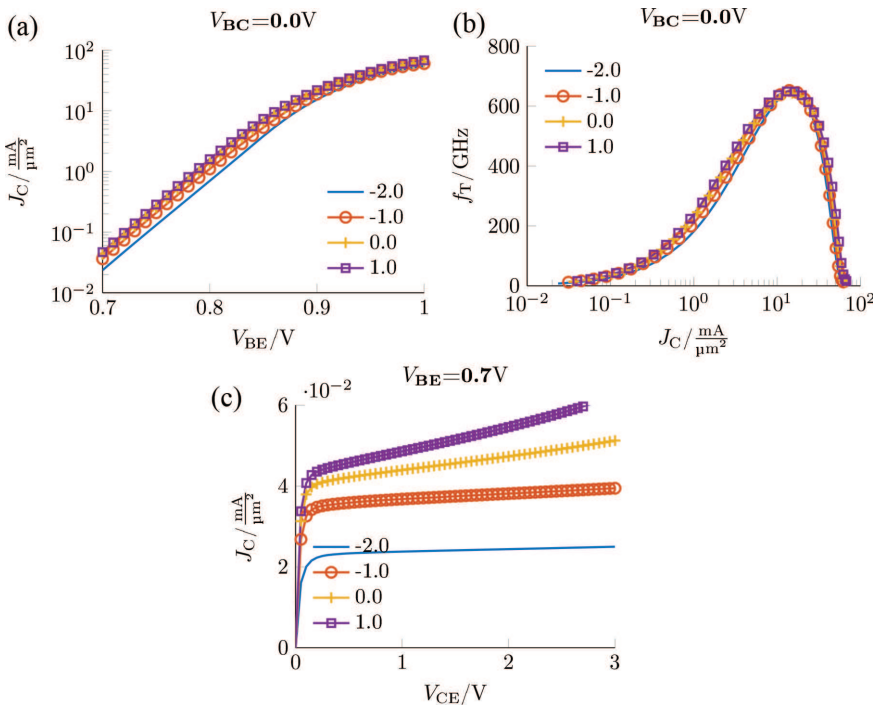

Figure 2.6 Illustration of the impact of f^{tc} on the transfer characteristic, transit frequency and output characteristics at $f^{\mathrm{td}} = f^{\mathrm{ec}} = 0$.

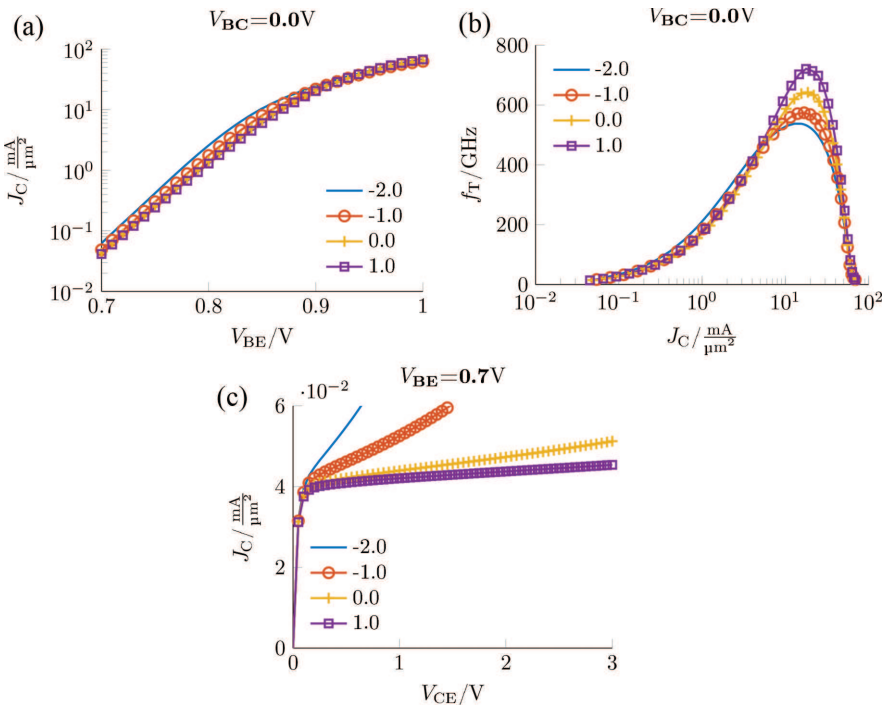

Figure 2.7 Exemplary illustration of the impact of f^{ec} ($f^{\mathrm{td}} = f^{\mathrm{tc}} = 0$) on the transfer characteristic, transit frequency and output characteristic.

The last HD transport model parameter f^{ec} scales the energy transport due to the current flow (see (2.29)). It has an opposite effect on the current density compared to f^{tc}, as shown in Figure 2.7. However, it allows to adjust the peak value of transit frequency ($f_{\mathrm{T,peak}}$).

The main burden for meaningful HD simulations is the determination of a proper set of HD transport model parameters. The following adjustment strategy and range of values proved to be suitable for the simulation of advanced SiGe HBTs:

- f^{td} is used for adjusting $J_{\mathrm{C}}(V_{\mathrm{BE}})$ and $f_{\mathrm{T}}(0.7 \leq f^{\mathrm{td}} \leq 2)$;
- f^{tc} prevents a negative output conductance $(-2.25 \leq f^{\mathrm{td}} \leq -1.75)$;
- f^{ec} is usually around zero $(-0.5 \leq f^{\mathrm{ec}} \leq 0.5)$.

Figure 2.8 compares the HD results obtained by the default HD model parameter set taken from SDevice [Syn15] with those obtained after adjustment to BTE results. The DD results are also shown for comparison.

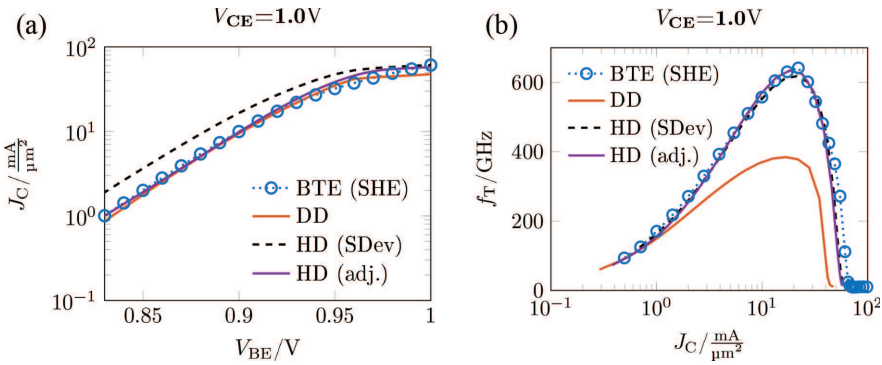

Figure 2.8 Transfer characteristic and transit frequency of the SiGe HBT in Figure 2.2 obtained from HD simulation with adjusted HD transport model parameters and SDevice defaults [Syn15], compared to BTE and DD simulation results.

Compared to DD, the HD transport model with the SDevice defaults gives already a good agreement for the transit frequency. However, the current densities are about twice as high as those obtained by the BTE and DD results. This discrepancy can be eliminated by adjusting the HD parameters to the BTE results. However, this agreement in the terminal characteristics is not reflected in the internal quantities (e.g. electron densities), which exhibit a different spatial dependence compared to the BTE results. In addition, there is no common set of HD parameters across technologies and generations in the same material. These parameters need to be readjusted for each major doping profile change in order to obtain reasonable results. Therefore, the computationally expensive BTE simulations are mandatory. In practice, it suffices though to simulate just the major technology nodes with the BTE and use those results to find the HD parameters for each node. With these parameters, HD simulations can then be applied for device optimization within a particular node [Wed10].

2.2.4.3 Effects beyond DD and HD transport

Due to the assumptions and simplifications involved in the derivation of the DD and HD transport models, some physical effects can not be captured by them compared to BTE solutions.

One assumption is the so-called single electron gas approximation [Blo70]. Here, the transport relevant electrons are assigned to one valley, which dominates the transport. In the case of silicon, the six valleys in Δ-direction (usually denoted by X-valleys) are combined to a single

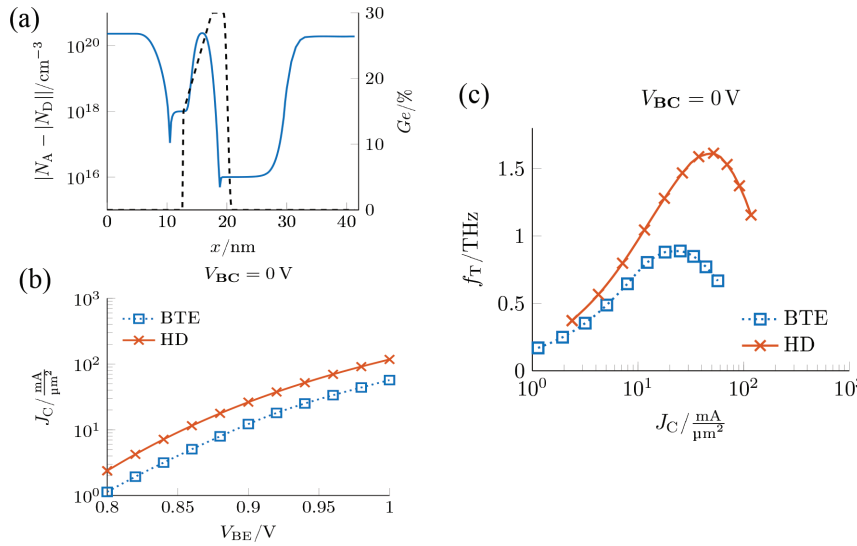

Figure 2.9 (a) Net doping and Ge profile of the SiGe HBT given in [Sch11] and the corresponding (b) transfer characteristic and (c) transit frequency obtained from BTE and HD simulation.

valley, which is energetically located at the conduction band edge. However, for SiGe and for material under biaxial-compressive strain, two of the six Δ-valleys are differently influenced with increasing Ge content [Hon11][Wed16]. In this case, two Δ-valleys are energetically shifted to higher potential energies, while the remaining four Δ-valleys undergo a downward shift in the potential energy. Hence, two conduction band edges are forming, where the lower conduction band edge is associated with the four and the higher with the remaining two valleys, respectively. In the case of DD or HD simulations, only the 4-fold lower conduction band edge is considered, neglecting the higher 2-fold conduction band edge. Figure 2.9 shows the impact of the neglected 2-fold conduction band for the SiGe HBT presented in [Sch11], which represents the presently known physical limit of SiGe HBT technology. According to Figure 2.9, the HD simulations overestimate both the collector current density and the peak transit frequency by about a factor of two. These discrepancies are caused by the abrupt rising edge of the Ge profile and the neglect of the second conduction band edge.

For clarification purposes, the band edges, valley occupancies and quasi-static electron densities at $f_{T,\,\mathrm{peak}}$ as obtained by BTE simulations are shown in Figure 2.10. Due to the abrupt rising edge of the Germanium profile, the

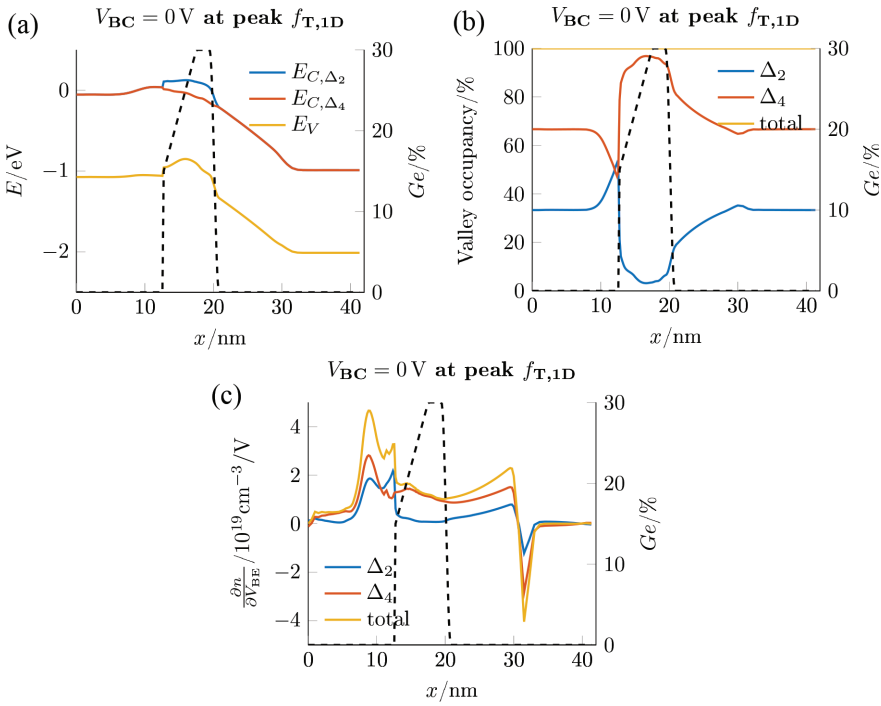

Figure 2.10 (a) Band edges and Ge profile, (b) valley occupancy, and (c) electron density of the SiGe HBT shown in Figure 2.9 obtained by BTE simulation at the operating point of peak transit frequency.

conduction band edge associated with the 2-fold Δ-valleys is energetically lifted up abruptly and thus forms an energy barrier (cf. Figure 2.10(a)). Only few high energetic electrons are able to overcome this barrier, while instead most of the electrons accumulate at the barrier (cf. Figure 2.10(b)). This leads to an additional charge, which reduces both the transit frequency and the transconductance [Hon11]. Obviously, the single electron gas approximation used in conventional DD and HD tools cannot capture this effect.

In fabrication, a step Ge profile is unrealistic and a graded profile rather occurs. The impact of a graded Ge profile is sketched in Figure 2.11. With the graded Ge profile (Figure 2.11(a)), the 2-fold Δ-valley is continuously shifted to higher energies so that the electrons are now able to gradually transfer to the 4-fold Δ-valley, preventing an abrupt charge accumulation (Figure 2.11(c)).

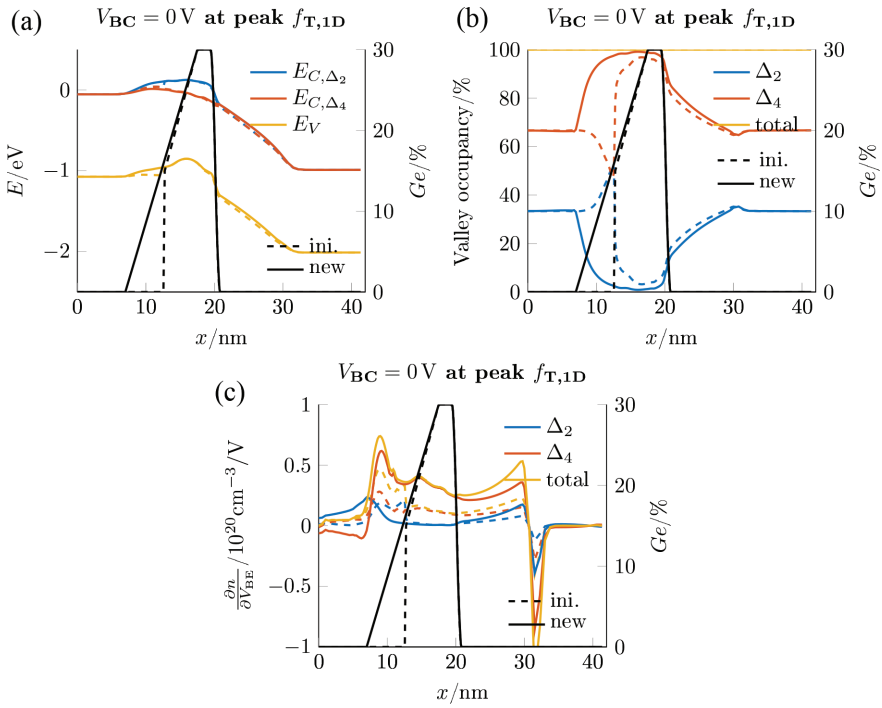

Figure 2.11 (a) Band edges and graded Ge profile as well as the corresponding (b) valley occupancy and (c) electron density obtained by BTE simulation at the operating point of peak transit frequency.

While the grading prevents a degradation of the transconductance, the higher quasi-static change of the electron density causes an increase of the total capacitance $\overline{C}_{\mathrm{tot}}$ connected to the base terminal. According to Figure 2.12(a), $\overline{C}_{\mathrm{tot}}$ increases by a factor of 1.76, whereas the transconductance $\overline{g}_{\mathrm{m}}$ improves by a factor of 2.57 (Figure 2.12(b)). Overall this leads to an increase of f_{T}. According to

$$f_{\mathrm{T}} = \frac{1}{2\pi} \frac{\overline{\overline{g}}_m}{\overline{C}_{\mathrm{tot}}}, \tag{2.30}$$

the higher improvement of the transconductance is resulting in an increase of f_{T} by a factor of 1.46.

Figure 2.13 shows the improvements in the collector current (Figure 2.13(b)) and in f_{T} (Figure 2.13(c)) due to the graded Ge profile.

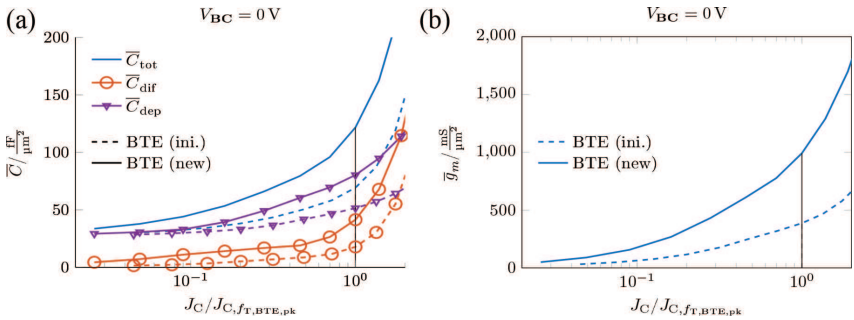

Figure 2.12 (a) Comparison of (a) the total 1D capacitance connected to the base node and its components and (b) the transconductance, obtained for the initial (abrupt) and the new (graded) SiGe HBT profile.

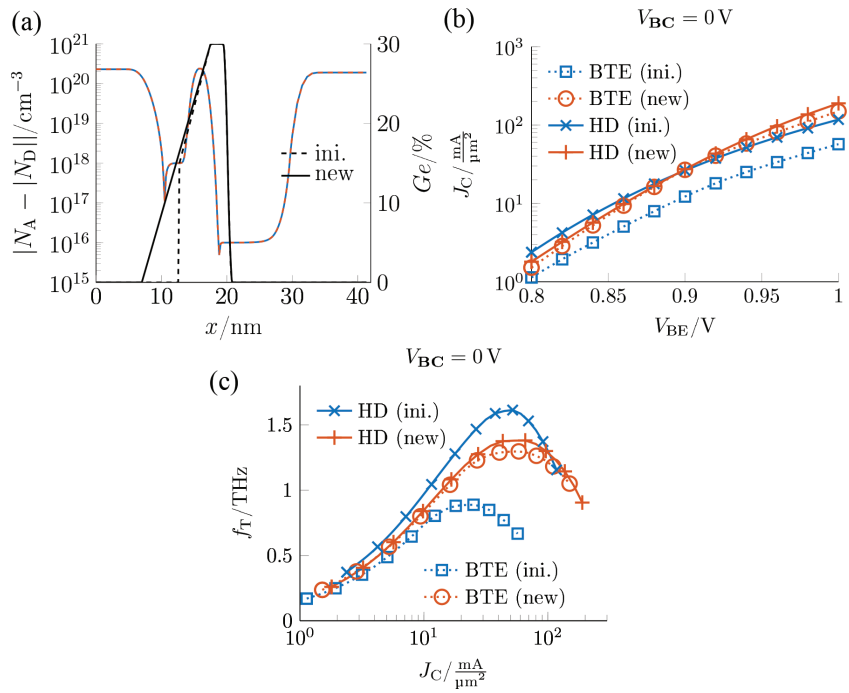

Figure 2.13 (a) Comparison of the initial and the new SiGe HBT profile with corresponding (b) transfer characteristic and (c) transit frequency, obtained by both BTE and HD simulation.

The good agreement of the HD results the with those of the BTE can only be obtained by readjusting the HD transport model parameters, since the Ge grading constitutes a major profile change.

Another limitation of the DD and HD transport model is the assumed shape of the distribution function for deriving them. Conventionally, a Maxwell-Boltzmann distribution is assumed over energy which, in the DD case, is assumed to be in equilibrium with the lattice or, in the HD case, has a modified decay over energy due the spatially dependent carrier temperature. However, in both cases a displacement of the distribution function off its equilibrium position is not considered. Contrary to DD and HD transport, the BTE is solved for the distribution function at each real-space point and over the reciprocal space and thus offers information about both the actual decay over energy and its displacement from the equilibrium position. Depending on the considered doping profile, different shapes of important characteristics can be obtained.

As an example, the SiGe HBT N3 in [Sch17] and shown in Figure 2.14(a) is considered. According to the transfer characteristics and transit frequency in Figure 2.14(b), (c), the deviations between HD and BTE occur despite

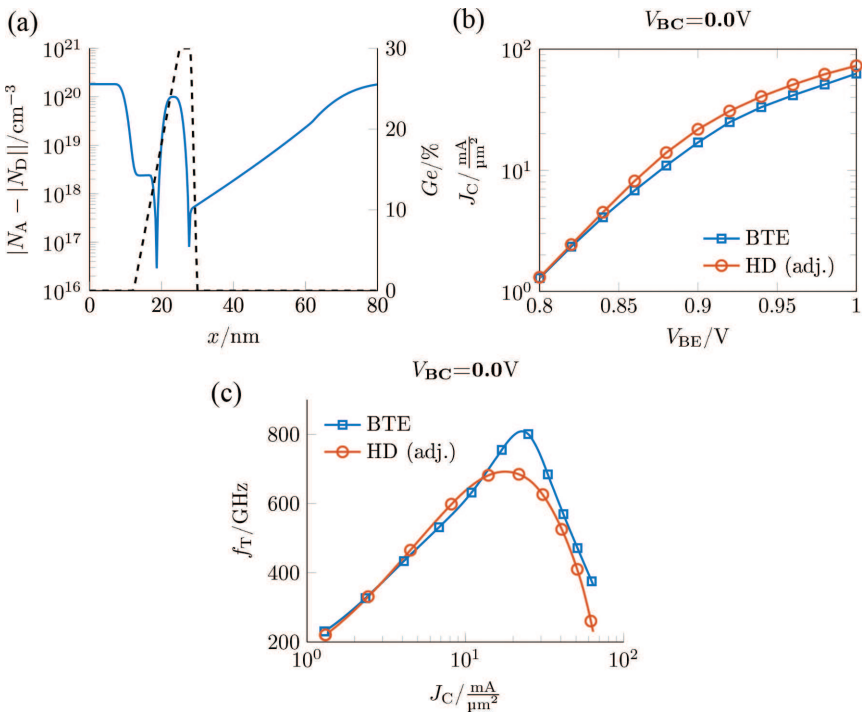

Figure 2.14 (a) Doping and Germanium profile of a SiGe HBT and the corresponding (b) transfer characteristic and (c) transit frequency obtained from BTE and HD simulation.

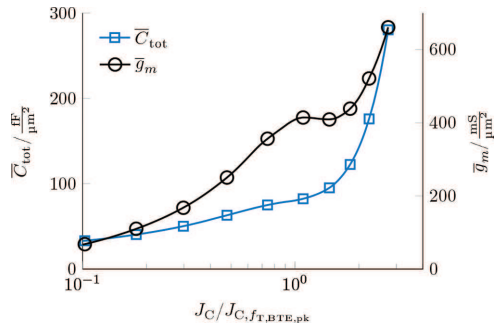

Figure 2.15 Transconductance and total capacitance of the N3 SiGe HBT.

adjusted HD transport model parameters. Especially for the transit frequency, the BTE predicts an spike-like increase to $f_{\rm T,BTE,pk}$ compared to HD transport. As explained below, the deviations between HD and BTE originate from the doping profile in conjunction with the doping dependent description of the bandgap narrowing and the subsequent shift of the conduction band edge.

In Figure 2.15, the bias dependent total capacitance and the transconductance of the N3 HBT are shown. According to (2.30), the spike-like increase in $f_{\rm T}$ originates from the strong increase and dip of the transconductance.

Since the electron transport within the device is dominated by the peak of the conduction band edge. The conduction band edge of the 4-fold Δ-valley and the contours of the corresponding electron distribution function for three different operating points are shown in Figure 2.16. Since the Pauli exclusion principle is not considered, the distribution function exhibits values larger than one (i.e. > 0 in Figure 2.16) near the conduction band edge in the highly

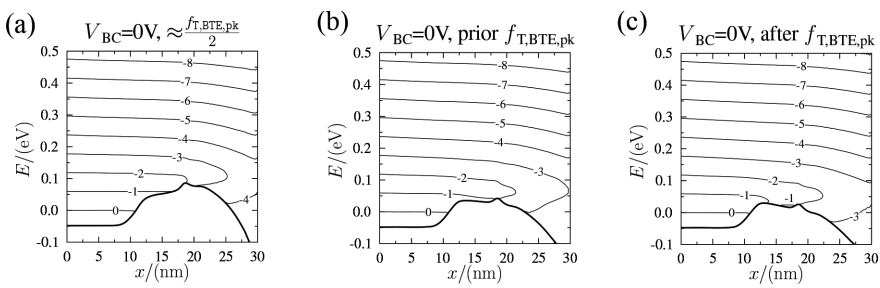

Figure 2.16 Conduction band edge versus location and superimposed contour lines of the (logarithm of the) electron distribution function of the 4-fold Δ-valley over energy within the emitter-base region for three operating points: (a) around $f_{\rm T,BTE,pk}/2$, (b) just before $f_{\rm T,BTE,pk}$, and (c) and just after $f_{\rm T,BTE,pk}$.

doped regions. As discussed before, the 4-fold Δ-valley carries by far most of the electrons and thus it is sufficient to focus on this valley only.

According to Figure 2.16(a) and (b), the conduction band peak for the current range up to around $f_{\mathrm{T,BTE,pk}}$ is located at $x = 19$ nm, which coincides with the steep doping gradient at the BE junction (see Figure 2.14(a)). This decrease in conjunction with the commonly employed (doping dependent) bandgap narrowing model [Slo77] leads to a sudden increase of the bandgap and consequently to a bias independent conduction band barrier, which is for the considered doping profile approximately 2.5 nm wide with a barrier height of around 10 meV. Due to the bending of the conduction band at higher applied V_{BE}-voltages, a plateau like conduction band edge is seen prior to $f_{\mathrm{T,BTE,pk}}$ in Figure 2.16(b). At an operating point beyond $f_{\mathrm{T,BTE,pk}}$ (see Figure 2.16(c)), a potential well is forming between x = 13 nm, which corresponds to the transition from the low to the highly doped emitter region and the associated bandgap difference, and $x = 19$ nm.

At current densities below $f_{\mathrm{T,BTE,pk}}$, only high energetic electrons can overcome the conduction band peak at x = 19 nm, which corresponds to the classical function of the V_{BE} modulated conduction band barrier that blocks, in the absence of tunneling, low energetic electrons. With increasing V_{BE} this barrier decreases and is overcome by a larger fraction of electrons. The resulting higher average electron velocity increases the current and transconductance and thus f_{T}. Around $f_{\mathrm{T,BTE,pk}}$, the bias independent conduction band peak x = 13 nm starts to get exposed and leads to a wider barrier region with a potential well enclosed. Beyond $f_{\mathrm{T,BTE,pk}}$, this wider barrier is more efficient in blocking the low energetic carriers. In addition, carriers also accumulate in the potential well, thus causing a rapid decrease of f_{T}.

In the case of the HD transport model, the Boltzmann distribution function is altered in its spread by the carrier temperature. But the behavior of low and high energetic electrons can still not be separated and thus the blocking effect of low energetic electrons around $f_{\mathrm{T,BTE,pk}}$ can not be captured. Figure 2.17(b) compares the assumed HD distribution function with the one obtained by the BTE solver. Compared to the BTE result, HD overestimates the low energetic and underestimates the high energetic electron population. Therefore, the hill observed in $\overline{g}_{\mathrm{m}}$ in Figure 2.15 originating from the increased average electron velocity at the conduction band peak is not observed in the DD or HD results, which are compared in Figure 2.18(a). Thus, the spike-like increase in $f_{\mathrm{T,BTE}}$ (see Figure 2.14(c)) can neither be reproduced by DD nor HD.

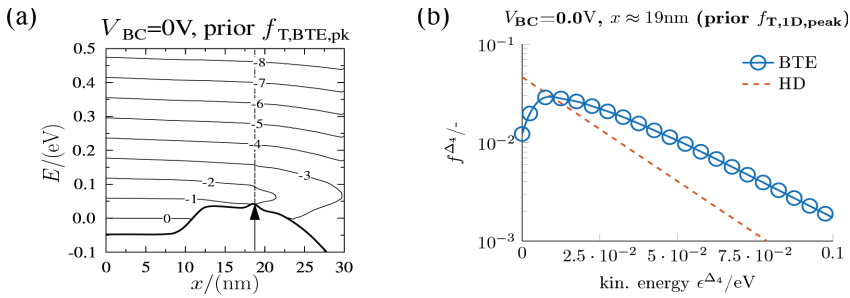

Figure 2.17 Electron distribution function within the 4-fold Δ-valley just below $f_{\mathrm{T,BTE,pk}}$ within the emitter-base region. (a) Contours with the arrow marking the position of the doping induced conduction band barrier. (b) Comparison of HD and BTE distribution function at the barrier.

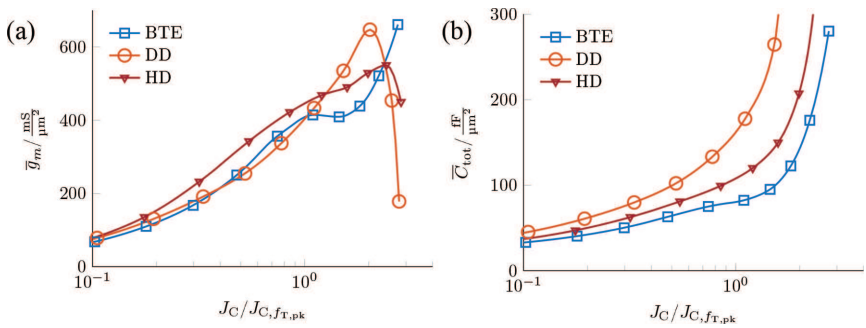

Figure 2.18 Comparison of (a) the transconductances and (b) the total capacitance obtained by DD, HD and BTE simulation results.

In addition and due to the missing energy separation, all DD or HD electrons participate to the charging of the capacitance, contrary to the BTE where the blocked low energetic carriers do not contribute. Thus, the DD and HD transport models are overestimating the total capacitance, as shown in Figure 2.18(b). A more detailed insight is given by Figure 2.19. Figure 2.19(a) compares the electron densities for the three considered operating points obtained by the BTE (lhs) and the HD (rhs) solver. Contrary to the HD results, only a slight variation of the electron densities within the lightly doped emitter is seen around $f_{\mathrm{T,BTE,pk}}$ due to the blocking of low energetic carriers. Since these blocked electrons do not participate to the charging of the dynamic capacitances, the quasi-static electron densities (dn/dV_{BE}) in the lightly doped emitter region are lower compared to those obtained by HD (see Figure 2.19(b)).

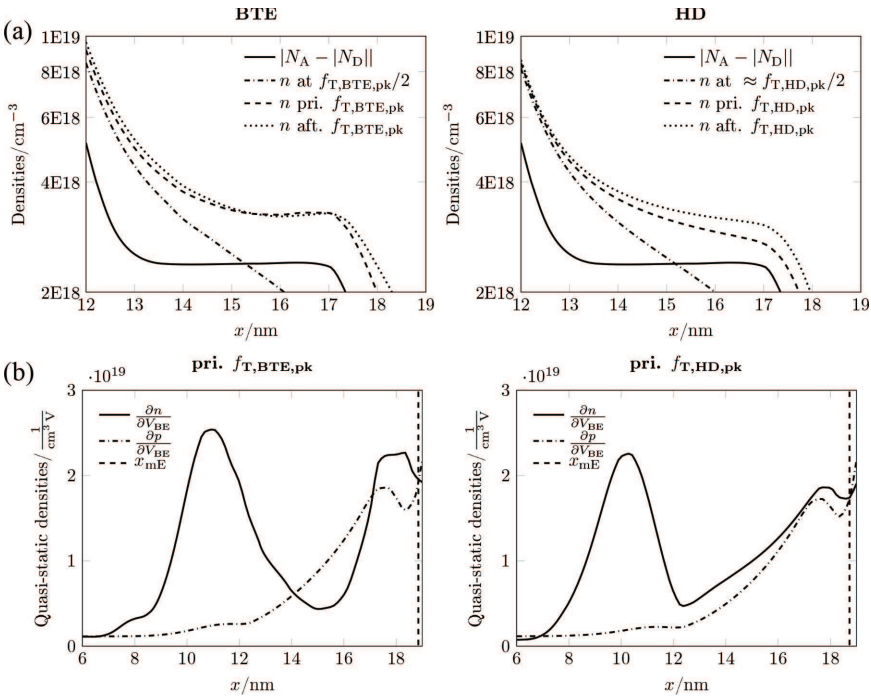

Figure 2.19 Comparison of the BTE and HD electron densities obtained by (a) an DC and (b) an quasi-static analysis. In (b), also the quasi-static hole densities are shown. For (b), a different axis intercept is used compared to (a) in order to visualize the contributions to the emitter junction capacitance $\overline{C}_{\mathrm{jEi}}$.

In terms of the emitter depletion capacitance [Sch06]

$$\overline{C}_{\mathrm{jEi}} = \int_0^{x_{\mathrm{mE}}} \frac{\partial}{\partial V_{\mathrm{BE}}}(n-p)\bigg|_{v_{\mathrm{BC}}} dx, \tag{2.31}$$

where $x_{\mathrm{mE}} = x(dn/dV_{\mathrm{BE}}{=}dp/dV_{\mathrm{BE}})$, the region of blocked electrons reduces the contributions to $\overline{C}_{\mathrm{jEi}}$ from the regions before, due to the higher quasistatic hole density (see Figure 2.19(b), lhs). Therefore, around $f_{\mathrm{T,pk}}$ the value of $\overline{C}_{\mathrm{jEi}}$ is overestimated in the HD results compared to the BTE results, as shown in Figure 2.20.

The spike-like increase discussed above has not been measured on fabricated devices, possibly because this effect might either be weakened due to tunneling or be masked by the impact of peripheral and external elements. In addition, the fabricated doping concentrations so far just do not have such a

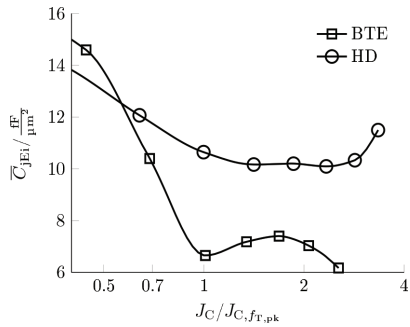

Figure 2.20 Comparison of $\overline{C}_{\mathrm{jEi}}$ obtained by BTE and HD simulations.

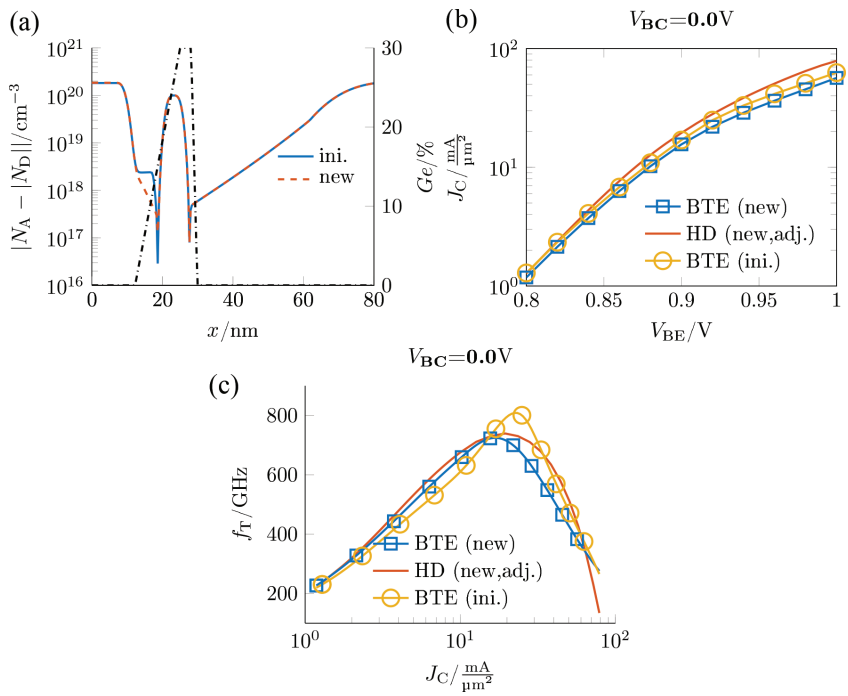

Figure 2.21 (a) Doping profile with smoothed high to low transition in the emitter (new) and previous step-like profile (ini.). Corresponding terminal characteristics: (a) transfer current and (b) transit frequency.

steep gradient. The latter hypothesis has been tested in Figure 2.21 showing a smoothed transition in the emitter doping (Figure 2.21(a)). This results in the disappearance of the previously observed peak f_T overshoot for the BTE

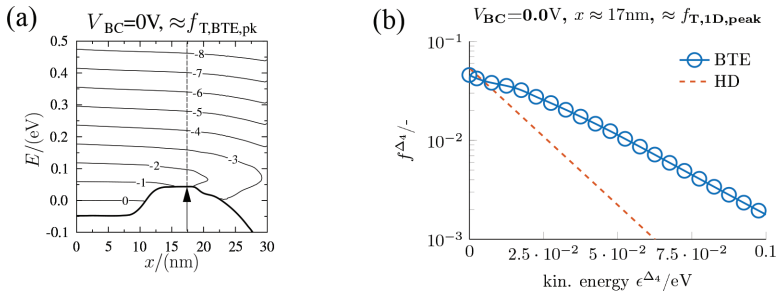

Figure 2.22 Electron distribution function within the 4-fold Δ-valley at $f_{\mathrm{T,BTE,pk}}$ within the emitter-base region. (a) Contours with the arrow marking the position of the doping induced conduction band barrier. (b) Comparison of HD and BTE distribution function at the barrier peak.

solver and terminal characteristics that are fairly close to the HD results (after adjusting though the HD transport model parameters (f^{td}, f^{tc} and f^{ec}).

In Figure 2.22(a), the conduction band edge and the contour lines of the electron distribution function for the smoothed doping profile are shown within the BE region. The corresponding distribution function in Figure 2.22(b) at the conduction band maximum at $x = 17$ nm shows no blocking of low energetic electrons and thus the HD and BTE results are approaching each other.

2.2.4.4 Comparison with experimental data

In the course of the DOTSEVEN project, a variety of experimental data of fabricated SiGe HBTs were evaluated. In order to evaluate the predictive capability of the TCAD infrastructure employed within the project, measured terminal characteristics, such as transfer current and f_{T} characteristics, were compared with simulation results. Here, a SiGe HBT fabricated by IHP and shown in Figure 2.23(a) is considered. For the comparison with the 1D simulation results, the measured data were deembedded by the external elements of the actual 3D transistor structure. This was accomplished by using the physics-based and geometry scalable properties of the HICUM/L2 compact model and its parameters, which were extracted from measured data of transistors and special test structures [Paw17][Kor15]. A comparison between the respective 1D measurements with the HD and BTE simulation results is given in Figure 2.23(b), (c) for the transfer current and transit frequency in the absence of self-heating, the impact of which has already been accounted for during the parameter extraction.

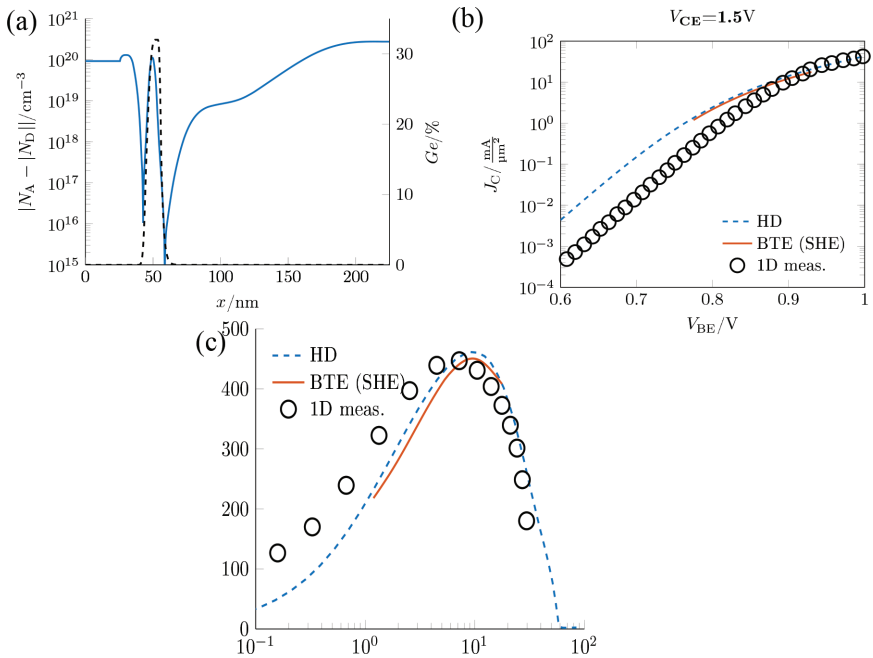

Figure 2.23 (a) Doping and Ge profile of a SiGe HBT (fabricated by IHP) with corresponding (b) transfer current, and (c) transit frequency. Comparison HD and BTE simulation results with 1D measurement data.

According to Figure 2.23(c), both HD and BTE simulation results agree well with the measured data around peak f_T and beyond. Below peak f_T, discrepancies exist which may be attributed to (i) too strong deembedding of parasitic or external junction capacitances in the measured data, (ii) an incorrect doping and Ge profile resulting in lower junction capacitances or doping and Ge dependent bandgap for the device simulation, (iii) the neglect of Carbon in the base region, or (iv) a significant difference in the doping, Ge and C dependent bandgap modeling in the simulation. The observed discrepancy in the transfer current (cf Figure 2.23(b)) indicates the latter as a major cause for the differences at low current densities.

According to Figure 2.24, the experimentally determined bandgap narrowing is indicating the presence of metastable strain, as reported in [Bea92]. For a first estimation of the impact of different bandgap narrowing values as function of Germanium on the terminal characteristics, a simple linear model ("lin." in Figure 2.24) is employed for DD and HD simulations. The corresponding terminal characteristics are shown in Figure 2.25.

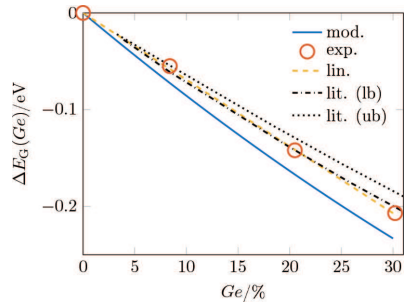

Figure 2.24 Comparison of the Ge concentration induced bandgap narrowing from experimental data (exp.) and device simulation model (mod.). In addition, the lower and upper boundary (lb and ub) for bandgap narrowing as function of Ge the presence of metastable strain [Bea92] is shown.

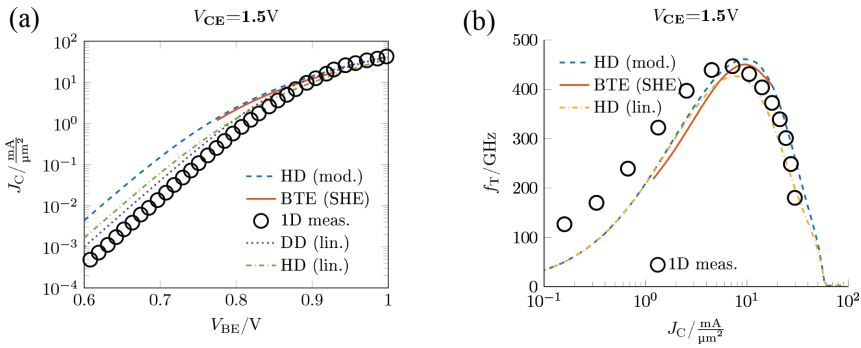

Figure 2.25 Comparison of the 1D measurement data with DD, HD and BTE simulation results. For the DD and HD simulation, the linear model indicated in Figure 2.24 is used. The transit frequency obtained by DD is not shown, since its parameters have not been adjusted.

According to Figure 2.25(a), the linear bandgap narrowing model improves the agreement between the simulated and experimental transfer characteristics at low current densities, but there is little improvement for f_T (cf. Figure 2.25(b)). Since advanced SiGe HBTs exhibit a significant carbon content, which is has not been considered in the simulations, further investigations based on experimental data (variation of the Germanium and carbon contents) are needed to clarify the origin of the discrepancies.

Nevertheless and focusing on trends only, the TCAD infrastructure employed in the DOTSEVEN project is capable of predicting performance trends correctly. Figure 2.26 displays the peak values of the measured 1D transit frequency for four different SiGe HBTs obtained from a process split. Here, both the quantitative and qualitative trend of the measurements is well

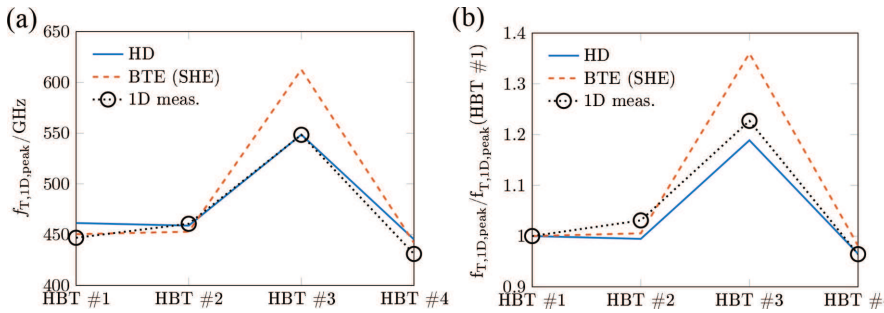

Figure 2.26 Comparison of the performance trends predicted by TCAD (HD and BTE simulation) with 1D measurement results (three samples) for a process split with four different SiGe HBTs (fabricated by HP).

captured by HD and BTE simulation. For the SiGe HBT labeled by HBT #3, the BTE results are overestimating the peak transit frequency. However, as explained before, this overestimation is based on an improper doping profile description at the metallurgical emitter-base junction and thus due to an underestimation of low energetic electrons.

2.3 Advanced Electro-thermal Simulation

C. Jungemann and N. Rinaldi

2.3.1 Carrier–Phonon System in SiGe HBTs

Charge carriers are accelerated under high electric fields in semiconductor devices and gain high kinetic energies. Carriers with energies higher than 60 meV scatter mainly with optical phonons. The optical phonons, which have a negligible group velocity, cannot participate in heat transport. Instead, they decay into long-wavelength acoustic phonons, which determine heat conduction in semiconductors. Since this decay is relatively slow, compared to the carrier–phonon interactions, a bottleneck for energy dissipation can occur, which results in a large number of hot optical phonons in high-field domains. The carrier–phonon and phonon–phonon interaction processes with their corresponding scattering time constants are illustrated in Figure 2.27 [Pop06].

In order to investigate self-heating in ultra-scaled bipolar transistors precisely, we have to consider a coupled system of transport equations for electrons, holes, and phonons. For this goal, the coupling terms, which describe carrier–phonon interactions, must be modeled accurately. In fact, carriers gain energy from the electric field and diffuse several mean free paths

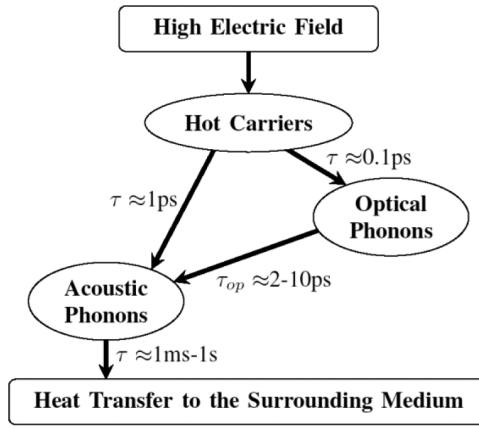

Figure 2.27 Thermal energy transport diagram in semiconductor devices.

(tens of nanometers) before they lose their energy to the lattice. Therefore, the so-called Joule-heating term, which represents the energy that carriers receive from the electric field, is not appropriate to capture the spatial distribution of heat generation in submicron devices. In order to tackle this problem, an advanced hydrodynamic model has been proposed [Mus08] to describe heat generation and transport in sub-micron silicon devices. However, this approach is still based on a single averaged carrier temperature within the relaxation time approximation and does not account for the spectral information regarding the emitted phonons. Since inelastic carrier–phonon scattering, which is described in detail by the scattering integral of the Boltzmann transport equation (BTE), causes heat generation, solving the BTE is the most accurate approach to study carrier–phonon interactions [Pop10].

The Monte Carlo (MC) method has been widely used to solve the BTE for electrons coupled with heat transport equations. The Fourier heat equation as the most elementary approach to consider heat conduction was used in [Zeb06, Sad10], which is not valid for sub-micron devices. In a CPU-efficient approach, a system of energy balance equations for both optical and acoustic phonons was extracted from the phonon BTEs. This system of equations coupled with an electron MC simulator, which was used to study self-heating in silicon-on-insulator devices, can describe the phonon bottleneck in thermal energy transport by distinguishing between optical and acoustic phonon temperatures [Ral08, Vas09]; however, it cannot capture all microscopic effects of non-equilibrium phonon transport due to the averaged phonon temperatures. Nghiem et al. [Ngh14] introduced recently an electrothermal simulator, which solves the BTE for both electrons and phonons

self-consistently. However, in their system of equations, the feedback to the electron system is the effective temperature extracted from the phonon distribution function.

Despite great advances in understanding the physics of phonon transport using the MC method, the stochastic basis of this method hinders calculation of parameters with very small or slow variations. Alternatively, a deterministic approach based on spherical harmonics expansion (SHE) can be used to solve the BTE [Gnu93]. In this regard, Ramonas et al. [Ram15] presented a deterministic solution of a non-equilibrium bulk electron–phonon system for noise calculations.

Most recently, Kamrani et al. [Kam17a] presented a SHE method for the coupled BTEs of electrons, holes, and phonons under stationary conditions in a SiGe HBT. Since it has been shown that carriers in SiGe lose their energy mainly by scattering with longitudinal optical (LO) phonons [Pop05, Ni12], they solved the phonon BTE only for the LO phonon mode, and used energy balance equations for the other optical and acoustic phonon modes. In addition, the reduction of the thermal conductivity in a SiGe HBT was accounted for by analytical models for the lattice thermal conductivity in a way that is consistent with empirical data.

2.3.2 Deterministic and Self-consistent Electrothermal Simulation Approach

In the framework of semi-classical transport theory, the kinetics of a non-equilibrium carrier–phonon system under stationary conditions is described by a coupled set of BTEs for the distribution functions of carriers (electrons/holes) $f^{e/h}(\overrightarrow{r}, \overrightarrow{k})$ and phonons $n(\overrightarrow{r}, \overrightarrow{q})$, defined on the position vector $\overrightarrow{r}$, carrier and phonon wave vectors $\overrightarrow{k}$ and $\overrightarrow{q}$, respectively. To investigate the impact of hot LO phonons on carrier transport, the non-equilibrium distribution function of LO phonons must be obtained, while for the other phonon modes, equilibrium distribution functions, which are evaluated at averaged phonon temperatures of the optical T_{op} and acoustic T_{ac} phonon branches, can be assumed. In this case, the BTE for the charge carriers is written as:

$$L\{f\} = Q^{LO}\{f, n\} + S\{f, T_{op}, T_{ac}\} \tag{2.32}$$

where $L\{f\}$ is the free-streaming operator, $Q^{LO}\{f, n\}$ is the scattering operator for inelastic interactions of carriers with non-equilibrium LO phonons, and $S\{f, T_{op}, T_{ac}\}$ denotes the scattering operator of all other

scattering mechanisms. The scattering term for non-equilibrium LO phonons is expressed as:

$$Q^{LO}\{f,n\} = \frac{V_0}{(2\pi)^3}\sum_{v'}\int\left[W^{v,v'}\left(\overrightarrow{r},\overrightarrow{k},\overrightarrow{k'},n\right)f^{v'}\left(\overrightarrow{r},\overrightarrow{k'}\right) - W^{v',v}\left(\overrightarrow{r},\overrightarrow{k'},\overrightarrow{k},n\right)f^{v}\left(\overrightarrow{r},\overrightarrow{k}\right)\right]d^3k' \tag{2.33}$$

where V_0 is the system volume, and $W^{v,v'}\left(\overrightarrow{r},\overrightarrow{k},\overrightarrow{k'},n\right)$ is the transition rate from the initial state $\left(v',\overrightarrow{k'}\right)$ into the final state $\left(v,\overrightarrow{k}\right)$ given by:

$$W^{v,v'}\left(\overrightarrow{r},\overrightarrow{k},\overrightarrow{k'},n\right) = C_0\left(\overrightarrow{r}\right)\left[n\left(\overrightarrow{r},\overrightarrow{q}\right)+\tfrac{1}{2}\mp\tfrac{1}{2}\right] \delta\left(\varepsilon\left(\overrightarrow{k}\right)-\varepsilon\left(\overrightarrow{k'}\right)\mp\hbar\omega_{op}\right) \tag{2.34}$$

where $C_0\left(\overrightarrow{r}\right)$ is the interaction constant, $\hbar\omega_{\mathrm{op}}$ is the constant energy for the dispersionless LO phonons, and the upper sign refers to phonon absorption and the lower to phonon emission.

The BTE for non-equilibrium LO phonons is written as:

$$\frac{n\left(\overrightarrow{r},\overrightarrow{q}\right)-n_{eq}(T_{\mathrm{L}})}{\tau_{op}} + G^c\{n,f\} = 0 \tag{2.35}$$

where the first term represents interactions between optical and acoustic phonons within the relaxation time (τ_{op}) approximation, $n_{eq}\left(T_{\mathrm{L}}\right)$ is the equilibrium phonon distribution function, which follows the Bose–Einstein statistics, T_{L} is the lattice temperature which is equivalent to the averaged acoustic phonon temperature, and $G^c\{n,\ f\}$ is the phonon generation term given by:

$$G^c\{n,f\} = \frac{2V_0}{(2\pi)^3}\sum_{v}\int\left[W^{v,v}_{ab}\left(\overrightarrow{r},\overrightarrow{k},\overrightarrow{q},n\right) - W^{v,v}_{em}\left(\overrightarrow{r},\overrightarrow{k},\overrightarrow{q},n\right)\right]f^{v}\left(\overrightarrow{r},\overrightarrow{k}\right)d^3k \tag{2.36}$$

where $W^{v,v}_{ab}$ and $W^{v,v}_{em}$ refer to the transition rate for phonon absorption and emission, respectively.

To solve this coupled system of BTEs, all the terms have to be expanded into spherical harmonics, and the spherical coordinates of the q-space

(q, θ_q, φ_q) can be expressed based on the modulus of the wave vector and the angles of the initial and final carrier states by using the momentum conservation rule, $\overrightarrow{k'} = \overrightarrow{k} \pm \overrightarrow{q}$.

In this simulation approach, non-equilibrium effects for the other phonon modes are accounted for by a coupled set of energy balance equations for the optical and acoustic phonon branches, where the energy loss rate due to inelastic carrier–phonon scattering is used as the heat generation term [Kam15]. Furthermore, the effects of Ge content [Pal04], doping profile [Lee12], and boundary scattering [Vas10] in the reduction of the lattice thermal conductivity, as the main parameter that models heat conduction by acoustic phonons, were considered via analytical models.

2.3.3 Hot Phonon Effects in a Calibrated System

To investigate non-equilibrium effects for the carrier–phonon system in bipolar transistors, a state-of-the-art toward-THz SiGe HBT fabricated by Infineon Technologies AG within the framework of the European DOTFIVE project with an emitter width of W_{E} = 0.13 μm and a length of L_{E} = 2.73 μm, and belonging to a technology development stage referred to as set #3 in [d'Al14], was used to extract the thermal resistance based on simple DC measurements. The extracted thermal resistance from measurements R_{TH} = 6,800 K/W [d'Al16] results in a junction temperature increase of $\triangle T_{\mathrm{j}}$ = 38.5 K at V_{BE} = 0.9 V and V_{CE} = 1 V with I_{C} = 5.66 mA.

To study self-heating in this device, 2-D electrothermal simulations were performed for the structure, which is partly shown in Figure 2.2, the doping profiles of which were extracted by secondary ion mass spectrometry (SIMS). For these simulations, a self-consistent steady-state solution of the BTEs for electrons, holes, and LO phonons coupled with the energy balance equations was obtained. Due to minor uncertainty in the extracted Ge profile, a calibration of the Ge content by a few percent is used to reproduce the measured I_{C} at T_{B} = 300 K by simulation. Figure 2.28 (top) depicts the thermal conductivity over the 2-D SiGe HBT by considering the effect of Ge content, doping concentration, and boundary scattering at 300 K.

Since the SHE solution of the BTEs for a 3-D real space is too CPU intensive, only a 2-D real space was used and some important parts of the structure for thermal conduction, such as metal layers, were neglected. To mimic the 3-D nature of the heat propagation in 2-D simulation, the thermal boundary conditions are adjusted to match the simulated average lattice temperature increase over the space-charge region of the base–emitter junction

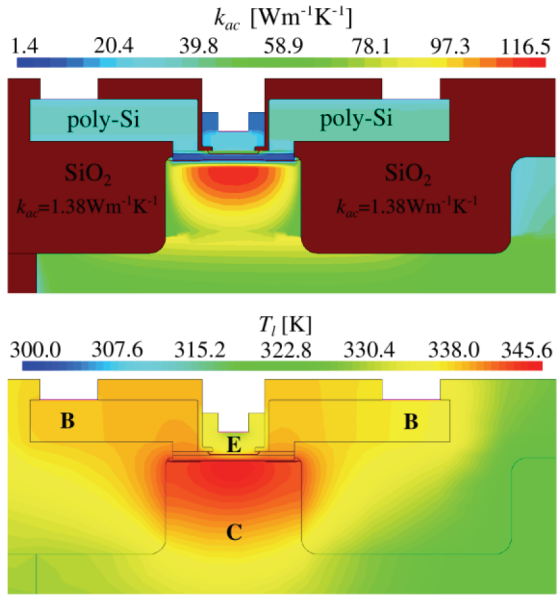

Figure 2.28 (Top) Thermal conductivity in the 2-D SiGe HBT structure by taking into account the effect of Ge content, doping concentration, and boundary scattering at 300 K. (Bottom) Self-consistent lattice temperature at V_{BE} = 0.9 V and V_{CE} = 1 V.

equal to the extracted junction temperature from measurements [d'Al02]. Hence, a convective boundary condition at the emitter contact is considered, and the heat transfer coefficient is calibrated to obtain an average junction temperature increase of 38.5 K from the temperature distribution of the simulation at the corresponding bias conditions. In this simulation, Neumann (adiabatic) boundary conditions are considered for artificial boundaries, the base and collector contacts, whereas the bulk contact at the bottom of the substrate is set to a constant temperature of 300 K. Figure 2.8 (bottom) shows the self-consistent lattice temperature obtained from the energy balance equations.

The spatial distribution of the Joule-heating term and the energy loss rate due to in-elastic carrier–phonon scattering are shown along the symmetry axis of the device in Figure 2.29. This figure depicts the distance that carriers have to travel before releasing their energy to the lattice; therefore, carriers receive energy from the high electric field at the collector–base junction, while they lose their energy via net phonon generation deep in the collector region. Moreover, Figure 2.29 shows that carriers are mainly scattered by

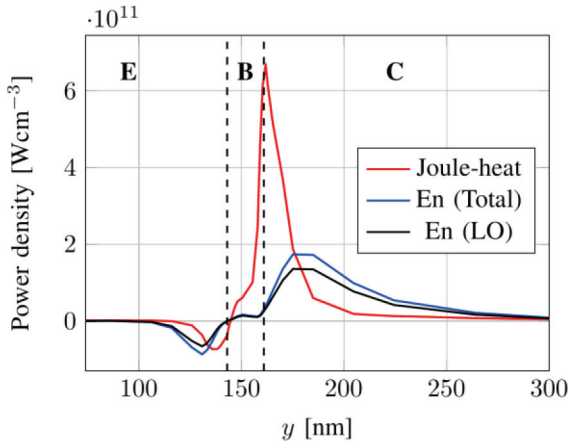

Figure 2.29 Profiles of the power densities received and dissipated by carriers which are calculated from Joule-heating and energy loss rate due to inelastic phonon scattering, respectively, along the symmetry axis of the HBT at V_{BE} = 0.9 V and V_{CE} = 1 V.

LO phonons which can lead to a strong deviation in the LO phonon distribution function with respect to the equilibrium value evaluated at the lattice temperature in the collector region which is shown in Figure 2.30 (top).

In order to investigate the effect of hot LO phonons and to make a comparison with the lattice temperature, an effective temperature is extracted from the non-equilibrium LO phonon distribution function which is shown in Figure 2.30 (bottom). The higher value of the effective temperature for LO phonons with respect to the lattice temperature, in the collector region, refers to the so-called phonon energy bottleneck in thermal conduction obtained for τ_{op} = 2 ps [Pop10]. The equality of T_{L} and T_{eff} around the base–emitter junction reveals the negligible effect of hot LO phonons on the collector current, because the temperature at this junction dominantly determines the impact of self-heating on the collector current increase. However, the large difference between these two temperatures in the collector region might influence some electrical phenomena, such as impact ionization (II) due to hot electrons, which occurs mainly deep in the collector region. To examine this possibility, the injected current due to electron II (I_{II}) was calculated in a simulation with high collector–base voltage V_{CB} = 2 V. A stronger phonon scattering due to hot LO phonons obtained from the full electrothermal simulation leads to a lower number of hot electrons. However, the reduction of the I_{II} at the same collector current due to temperature increase is just a few percent. As a result, the impact of hot LO phonons on electron II is not very strong in this case.

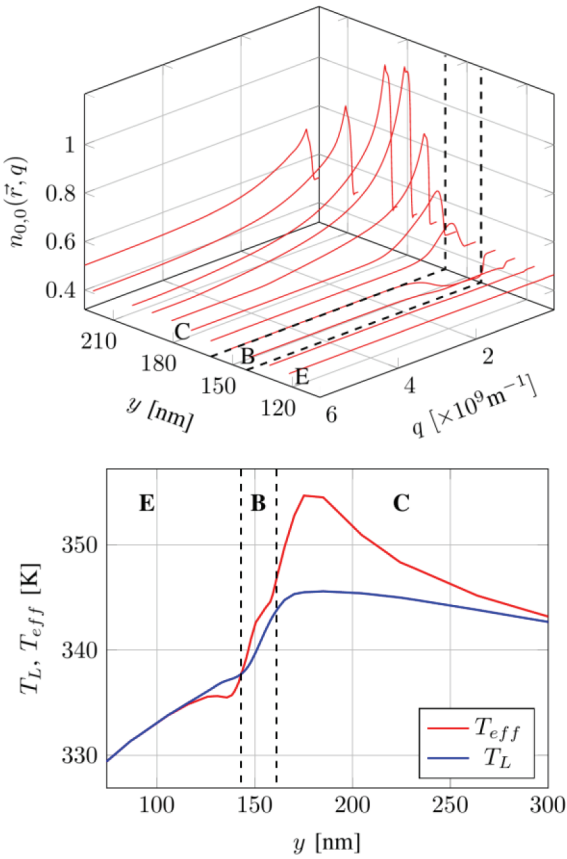

Figure 2.30 (Top) The LO phonon distribution function (zeroth-order harmonic), and (bottom) lattice temperature and effective temperature for LO phonons, along the symmetry axis of the investigated HBT at V_{BE} = 0.9 V and V_{CE} = 1 V.

2.3.4 Thermal Resistance Extraction from the Simulated DC Characteristics

To extract the thermal resistance by an approach similar to the experimental extraction method [d'Al14], the required DC characteristics were calculated and compared with measurement data (Figure 2.31). Figure 2.31 (top) displays the $I_{\mathrm{C}} - V_{\mathrm{BE}}$ characteristics of the HBT at different homogeneous temperatures, compared to experimental data measured under DC conditions at various thermo-chuck temperatures. In these voltage/current ranges, self-heating can be safely disregarded and the results are used for calculating the

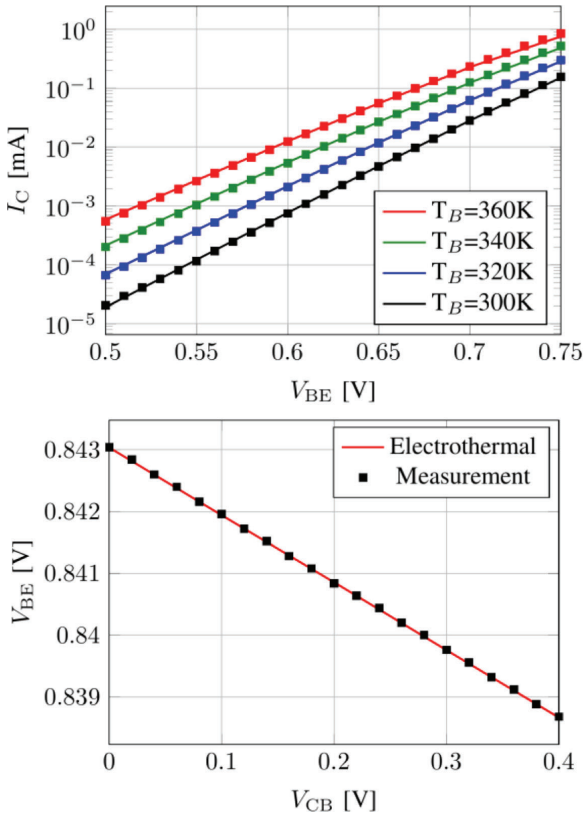

Figure 2.31 (Top) $I_C - V_{BE}$ characteristics for different homogeneous temperatures at V_{CE} = 0.6 V. Solid lines show the isothermal simulation results at T_B = 300, 320, 340, 360 K and symbols show the corresponding measurement data. (Bottom) $V_{BE} - V_{CB}$ characteristics from electrothermal simulation and measurement at I_E = 2 mA.

temperature coefficient $\varphi = -(\partial V_{BE}/\partial T_B)|_{I_C}$. The extraction of the other parameter $\gamma = (\partial V_{BE}/\partial V_{CB})|_{I_E}$ can be troublesome with the MC method, because the variation of V_{BE} with respect to V_{CB} for a constant I_E is very small. Moreover, thermal parameters of the device determine the slope of the $V_{BE} - V_{CB}$ curve [Kam15]; consequently, a self-consistent electrothermal simulation is needed to evaluate the slope of this curve consistent with the lattice temperature distribution of the device. Figure 2.32 shows the $V_{BE} - V_{CB}$ characteristics obtained from the deterministic and self-consistent electrothermal simulator in comparison with the measurement data.

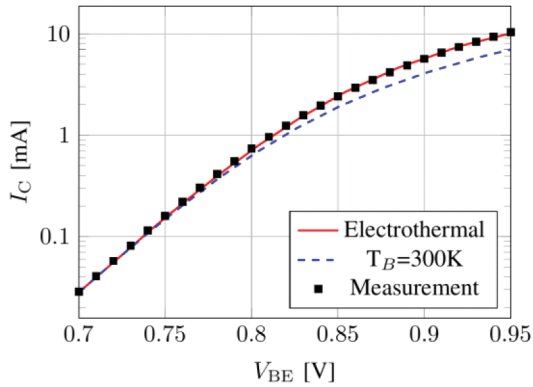

Figure 2.32 $I_C - V_{BE}$ characteristics with and without including self-heating compared to measurement data at V_{CE} = 1 V.

Since the simulated DC characteristics are in very good agreement with measurement results, the extracted thermal resistance from electrothermal simulations $R_{TH} = -\gamma/(I_E\varphi)$ matches the value obtained from measurements. This confirms the consistency of the extracted junction temperature from the simulated DC characteristics with the average lattice temperature over the base–emitter junction observed in the temperature profile shown in Figure 2.30 (bottom). Therefore, this result attests the accuracy of the analytical model on which the experimental procedure is based.

Figure 2.32 shows the effect of self-heating on the collector current increase observed in $I_C - V_{BE}$ characteristics of the SiGe HBT by electrothermal SHE simulations, which matches measurement results very well.

2.4 Microscopic Simulation of Hot-carrier Degradation

2.4.1 Physics of Hot-carrier Degradation

Due to inevitable trade-offs in the performance optimization of SiGe HBTs, these devices are operated closer and even beyond the classical safe-operating area (SOA) borders. Hot-carrier degradation (HCD) is the main reliability concern in bipolar transistors that strongly limits the lifetime of a device operated close to the SOA limit [Fis15]. This degradation happens due to trap states generated by hot-carriers along the oxide interfaces over time. In general, imperfections at the Si/SiO_2 interface lead to silicon dangling bonds, which can capture electrons or holes. Hence, these dangling bonds

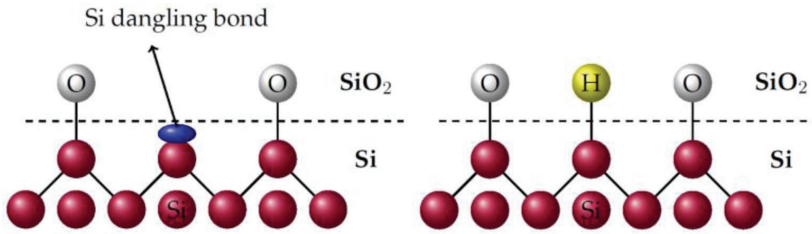

Figure 2.33 (Left) Creation of Si dangling bonds at the Si/SiO_2 interface. (Right) Passivation of the dangling bonds by incorporating hydrogen atoms.

are intentionally passivated by incorporating hydrogen atoms (Figure 2.33). However, hot carriers can supply enough energy to break the passivated Si–H bonds. A hot-carrier is a charge carrier which is accelerated under a high electric field inside the device and attains significant kinetic energy (higher than 1.5 eV) to break the bonds directly. Therefore, devices operating under bias conditions, which produce large electric fields, are susceptible to the HCD phenomenon.

In high-performance HBTs, shallow trench isolation (STI) and deep trench isolation (DTI) schemes together with the emitter–base (EB) spacer oxide are used to reduce parasitic capacitances and leakage currents [Mar09]. However, trap states resulting from the Si–H bond dissociation at the EB spacer and STI oxide interfaces produce excess non-ideal base current via Shockley–Read–Hall (SRH) recombination in the forward mode and reverse mode, respectively (Figure 2.34). As a result, traps generated due to hot carriers along the EB spacer oxide interface degrade the main parameters of

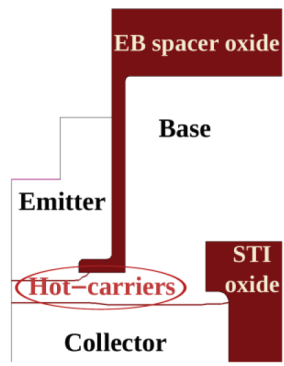

Figure 2.34 Schematic of a state-of-the-art SiGe HBT with the corresponding EB spacer and STI oxides.

the device such as current gain and noise figure [Cre04]. Hence, a profound knowledge of the microscopic mechanisms of the interface trap generation and annihilation as well as their impact on the electrical characteristics is essential.

Although conventional methods for a physics-based investigation of HCD in bipolar transistors, which are based on the lucky electron model, are electric field driven [Che09, Moe12, Wie16], it has been shown that the trap generation rate at the oxide interface is determined by the energy of the interacting charge carriers [DiM89, DiM01]. Hence, another quantity called the acceleration integral (AI), which is calculated from the carrier energy distribution function (EDF), has been introduced to describe accurately the spatial distribution of the interface traps obtained from charge pumping measurement data [Sta11, Sta12]. In consequence, an energy-driven paradigm based on the AI has been developed to model both single- and multiple-carrier processes of the bond dissociation in the degradation analysis of the n-channel MOSFETs [Bin14, Sha15, Tya16].

This model has been recently extended to include the effects of both hot electrons and hot holes for describing the underlying mechanisms of HCD in bipolar transistors [Kam16, Kam17b]. For this purpose, a coupled system of BTEs for electrons and holes, which accounts for II and SRH, has to be solved. Since stochastic algorithms such as the MC method impose an enormous computational burden to resolve the high-energy tail of the EDF, a deterministic approach based on a SHE was used to solve the BTEs including full band structure effects [Hon11].

The reaction-diffusion model has been widely used to represent the complex dynamics of the trap generation and subsequent annihilation in HCD of bipolar transistors and negative-bias temperature-instability degradation of MOSFETs [Moe12, Rag15, Kuf07]. Despite a very good matching for a wide range of experimental observations, it has been shown that the reaction-diffusion model is inconsistent with the measurement data at the microscopic level [17]. Therefore, in [Kam17b] a degradation model based on the AIs was used to calculate the dispersive bond-breakage rates associated with a reaction-limited model to describe HCD effects in a SiGe HBT.

2.4.2 Modeling of Hot-carrier Effects

In an energy-driven framework, the bond-breakage rate is modeled by considering the interaction of the incident charge carriers with the passivated Si–H bond. A Si–H bond is represented as a truncated harmonic oscillator

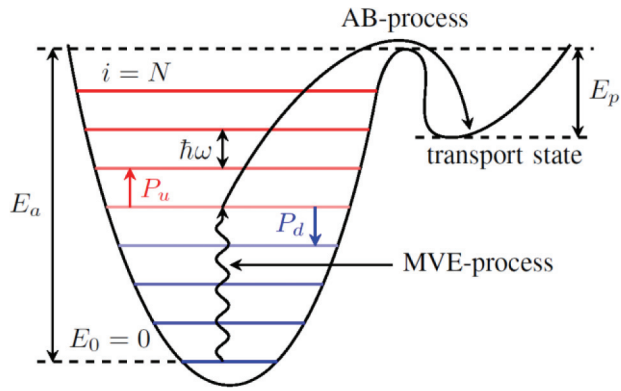

Figure 2.35 The energy configuration of the Si–H bond modeled as a truncated harmonic oscillator.

characterized by a system of eigenstate energies [Sto98], which is depicted in Figure 2.35.

Bond dissociation occurs via excitation of one of the bonding electrons to the transport state, which is known as an antibonding (AB) process. As a result, a repulsive force is induced, which detaches the hydrogen atom. The dissociation rate from the ith state of the Si–H bond with the energy E_i, triggered either by a hot electron or by a hot hole, is given by:

$$R_{AB,i} = I^e_{AB,i} + I^h_{AB,i} + \upsilon_r \, \exp\left(-(E_a - E_{ox}d - E_i)/k_B T_0\right) \qquad (2.37)$$

where $I^e_{AB,i}$ and $I^h_{AB,i}$ are the AB acceleration integrals of electrons and holes, respectively, υ_r is an attempt frequency, and E_a is the bond-breakage activation energy, which is reduced due to the interaction of the bond dipole moment d with the oxide electric field E_{ox}. Furthermore, to account for the fluctuations of the activation energy, a Gaussian distribution is considered with a mean value and standard deviation of $\langle E_a \rangle$ and σ_E, respectively. The AI for the AB process is given by [Bin14]

$$I^{e/h}_{AB,i} = \sigma_0^{AB} \int_{E_{th,i}}^{\infty} \left[f^{e/h}(E)\, z^{e/h}(E)\, v_g^{e/h}(E) \left[(E - E_{th,i})/E_{ref}\right]^p \right] dE \qquad (2.38)$$

where $E_{th,i} = E_a - E_{ox}d - E_i$ is a threshold energy for the ith level, σ_0^{AB} is the AB reaction cross section, $f^{e/h}(E)$ is the carrier distribution function, $z^{e/h}(E)$ is the carrier density of states, $v_g^{e/h}(E)$ is the carrier group velocity, $p = 11$ is an empirical parameter, and $E_{ref} = 1\text{eV}$.

If a charge carrier does not provide enough energy to trigger the AB mechanism, it can still contribute to the bond-breakage procedure via multiple vibrational excitation (MVE) of the bond. In an accumulative consideration of the MVE and AB mechanisms, the bonding electron can be firstly excited by several colder particles to an intermediate energy level, and then dissociated by a carrier with a relatively high energy. The bond excitation and deexcitation rates triggered by either a cold electron or a cold hole, are given, respectively, by

$$P_u = I^e_{MVE} + I^h_{MVE} + \omega_e \ \exp\left(-\hbar\omega/k_B T_0\right) \tag{2.39}$$

$$P_d = I^e_{MVE} + I^h_{MVE} + \omega_e \tag{2.40}$$

where ω_e is the reciprocal phonon life-time and $\hbar\omega$ is the energy distance between the Si–H energy levels. The AI for the MVE process is defined as

$$I^{e/h}_{MVE} = \sigma_0^{MVE} \int_{\hbar\omega}^{\infty} \left[f^{e/h}(E)\, z^{e/h}(E)\, v_g^{e/h}(E) \left[(E-\hbar\omega)/E_{ref}\right] \right] dE \tag{2.41}$$

The cumulative bond-breakage rate, which accounts for all possible superpositions of the AB and MVE mechanisms, is calculated as

$$R_a = \tfrac{1}{k} \sum_i R_{AB,i} \left(\tfrac{P_u}{P_d}\right)^i \tag{2.42}$$

where k is a normalization prefactor defined as $k = \sum_i \left(P_u/P_d\right)^i$.

In the reaction-limited approach, the rate equation for the generation and recombination of the interface trap states is written as [Jep77]

$$\partial N_{it}/\partial t = \left(N_0 - N_{it}\right) R_a - {N_{it}}^2 R_p \tag{2.43}$$

where N_{it} is the density of the generated interface traps, N_0 is the density of the primary passivated Si–H bonds, and R_p is the recovery rate.

In this approach, the dispersion of the bond-breakage energy determines the power-law time dependence of the HCD results. The dispersive effect of E_a is incorporated by discretizing an energy grid in the range of $[\langle E_a\rangle - 3\sigma_E, \langle E_a\rangle + 3\sigma_E]$ and evaluating Nit for each discretization point. The interface trap density profile, which is the combination of every single defect, is obtained by calculating the average of Nit at each energy point weighted by the Gaussian distribution [Bin14].

To obtain the required distribution functions of the carriers, a coupled system of the BTEs for electrons and holes has to be solved. The BTE for electrons in the stationary case is written as:

$$L\left\{f^e\right\} = S\left\{f^e\right\} + Q\left\{f^e, f^h\right\} - \Gamma^e\left\{f^e, f^h\right\} \tag{2.44}$$

where $S\{f^e\}$ is the scattering operator, which accounts for carrier–phonon scattering, impurity scattering, alloy scattering, and II scattering of primary particles, $Q\left\{f^e, f^h\right\}$ is the generation operator of secondary particles due to II [Jab14], and $\Gamma^e\left\{f^e, f^h\right\}$ is the SRH recombination operator [Jun07, Rup16] defined on the boundary of the oxide interface.

In this simulation approach, a full-band SHE simulator is used to obtain the carrier EDFs for a SiGe HBT under stress conditions. Then, the $N_{it}\left(\overrightarrow{r}, t\right)$ profile calculated at each stress time step is fed into the SHE solver to calculate the characteristics of the degraded device which change due to SRH recombination.

2.4.3 Simulation of SiGe HBTs under Stress Conditions Close to the SOA Limit

The conventional mixed-mode (MM) stress conditions, which are the concurrent applications of a high collector-base voltage and a high collector current density to accelerate the degradation procedure, set an upper limit for HCD of the SiGe HBTs during RF operation [Fis15]. However, as the main drawback they are far from typical operating conditions. Hence, to study the physics behind the long-term base current degradation under more practical operating conditions, three stress bias conditions P1, P2, and P3, along the border of the SOA, were selected to degrade the device up to 1,000 h at 300 K, and Gummel plots (V_{CB} = 0 V) were measured at certain stress time intervals [Jac15]. The corresponding bias voltage, current, and junction-to-ambient temperature increase obtained from the extracted thermal resistance R_{TH} = 2,850 K/W [d'Al14] are summarized in Table 2.1. Measurements showed that the examined npn SiGe HBT is negligibly affected by stress at P1, and P3 exhibits a higher base current degradation over time in comparison to P2.

For numerical simulations, a 2-D structure, the doping profiles of which were extracted from SIMS, was used. As a first step of this analysis, the simulator has to be calibrated to reproduce the measured Gummel plot and $I_{\mathrm{B}} - V_{\mathrm{CE}}$ characteristics of the fresh device. The base current reversal at

Table 2.1 Definition of the stress bias conditions P1, P2, and P3 and their corresponding junction temperatures

	P1	P2	P3
V_{CE} [V]	1 ($<BV_{\mathrm{CEO}}$)	2 ($>BV_{\mathrm{CEO}}$)	3 ($>BV_{\mathrm{CEO}}$)
J_{C} [mA/μm^2]	10	5	1
ΔT_{j} [K]	37	37	11

$V_{CE}>BV_{CEO}$ due to avalanche multiplication of carriers is used as a basis to determine the II rates initiated by primary electrons and holes. Figure 2.36 shows the II generation rates at P3 due to electrons and holes separately.

Under this stress condition, the high electric fields within the collector–base junction accelerate electrons to reach enough energy required for initiating avalanche generation of electron–hole pairs via II. Figure 2.36 shows that hot electrons responsible for II are deep in the collector region while hot holes are mainly found in the base region. To obtain a better understanding of the energy of the carriers which participate in the degradation process, Figure 2.11 depicts a cut of the EDFs for electrons and holes along the symmetry axis of the investigated SiGe HBT with respect to kinetic energies.

Electrons move toward the collector region and gain sufficiently high energies to initiate II, whereas the holes generated by II in the collector due to hot electrons [Figure 2.36 (top)] are accelerated toward the base and gain a lot of energy. Due to this high energy, some of the holes can shoot through

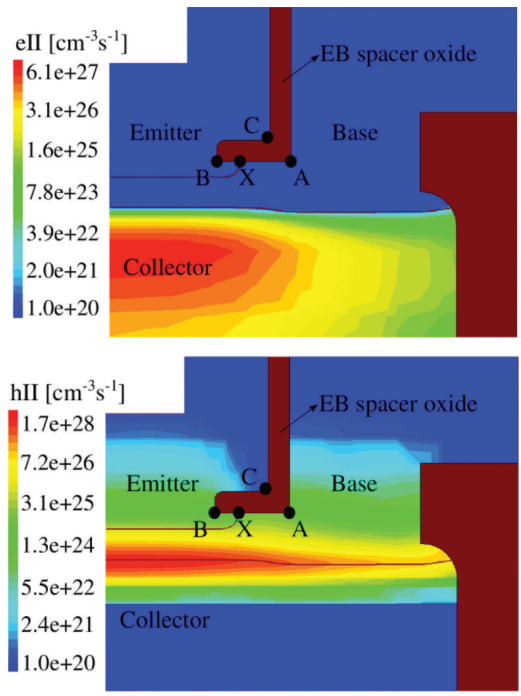

Figure 2.36 II generation rates in the SiGe HBT induced by electrons (top) and holes (bottom) at P3.

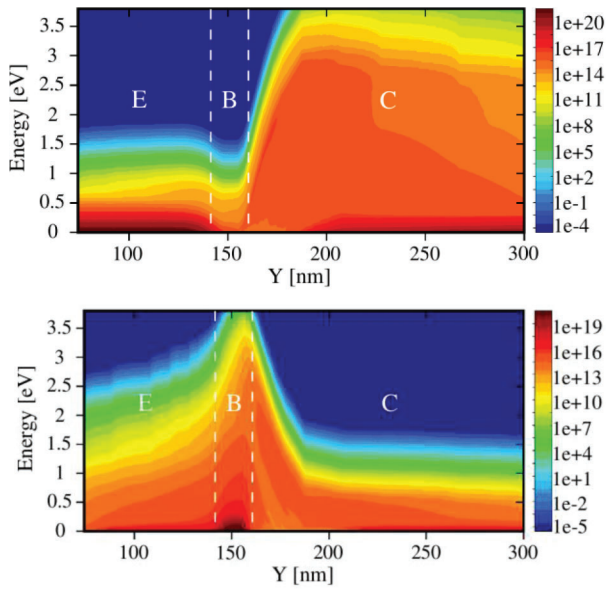

Figure 2.37 Cut of EDFs [eV^{-1} cm^{-3}] for electrons (top) and holes (bottom) along the symmetry axis of the HBT at P3.

the base into the emitter, where they still have a relatively large energy [Figure 2.37 (bottom)]. A certain fraction of these hot holes hit the EB spacer oxide interface, where they might break Si–H bonds.

This effect can only be captured by a model which resolves the dependence of the carriers on energy. Thus, it is not possible to directly describe the behavior of the hot holes with a drift-diffusion or a hydrodynamic model, in which the hole gas in the base is assumed to be close to equilibrium. Unavoidably, to perform physics-based degradation analysis relying on the classical models, the probability of hot carrier creation has to be calculated via the lucky electron model. This calculation based on the effective electric field shows inaccurately that hot holes are found at the collector–base junction. Subsequently, the possibility that a hot carrier reaches the oxide interface without any deflection has to be separately estimated [Moe12].

The interface traps located within the EB space-charge-region have the highest impact on the forward mode base current degradation via SRH recombination. Therefore, the EDFs at the intersection of the EB junction and the oxide interface are compared for different stress conditions in Figure 2.38 (top). The negligible role of electrons in the degradation process

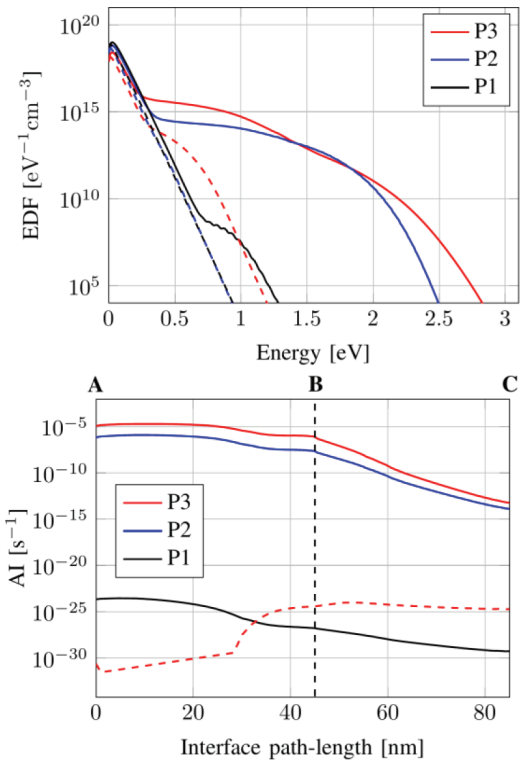

Figure 2.38 (Top) EDFs of electrons (dashed lines) and holes (solid lines) at the intersection of the EB spacer oxide interface and the EB junction [denoted by node X in Figure 2.36 (Bottom)]. Profiles of the AB AIs for electrons (dashed lines) and holes (solid lines) along the EB spacer oxide interface from node A to C denoted in Figure 2.36.

is concluded from the EDFs for electrons at P1 and P2, which exactly follow the equilibrium EDF, and at P3, with a low-energy hump. Because of small collector–emitter voltage in P1, even holes do not gain high energies, which explains the negligible degradation rate at P1 observed in measurements. Furthermore, the high-energy tails of the hole EDFs at P2 and P3 reveal the dominant role of hot holes in the degradation process under the stress conditions close to the SOA limit, which was also reported for conventional MM stress conditions in [Van06]. However, the deterministic solver provides the possibility to comprehensively describe the microscopic effects of hot carriers and accurately obtain the EDFs up to high energies in a realistic 2-D device structure and develop a practical physics-based degradation model to evaluate the resulting excess base current.

Although cold carriers can also participate in the MVE of the Si–H bonds, hot carriers with energies greater than 1.5 eV have a much higher chance to break the Si–H bonds directly [Tya16]. Moreover, the activation energy parameters determine the power-law time dependence and the dependence of the excess base current on the stress conditions. Hence, $\langle E_a \rangle$ = 1.6 eV and σ_E = 0.2 eV, which are in good agreement with those experimentally obtained [Ste96, Pob13], were considered for the activation energies of the bond-breakage to achieve good agreement with measurement data.

The AB AIs along the EB spacer oxide interface obtained from this calibration are depicted in Figure 2.38 (bottom). As an expected result, the equilibrium electron EDFs at P1 and P2 result in zero AB AIs along the oxide interface. Furthermore, due to the low-energy humps in the EDFs of electrons at P3 and holes at P1, their corresponding AIs are very small. In consequence, the measured base current degradations under P2 and P3 have to be ascribed to hot holes with relatively high AB rates, in which the bigger AI at P3 compared to P2 explicitly explains the bigger degradation current under this stress condition.

Figure 2.39 represents the trap densities along the EB spacer oxide interface for several stress time steps, which are significantly generated by the AB process due to hot holes. These interface trap densities, calculated for $N_0 = 10^{12}$ cm^{-2}, reveal that the large variation of the AB AIs along the oxide interface results in a strong non-uniformity in the spatial distribution of the N_{it} profile.

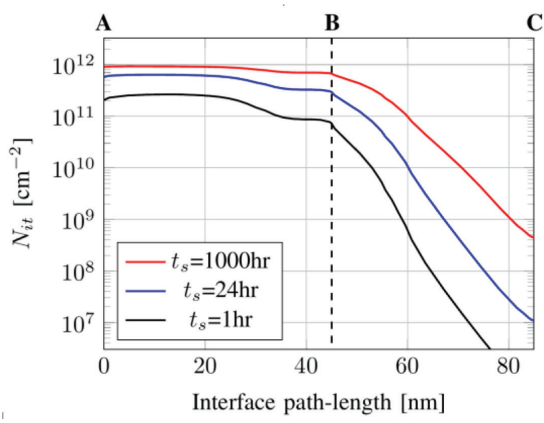

Figure 2.39 Interface trap densities generated at different stress time steps from node A to C denoted in Figure 2.36 at P3.

The generated traps at the EB spacer oxide interface cause a non-ideal increase in the forward mode base current via field-enhanced SRH recombination [Hur92]. Figure 2.14 (top) shows the Gummel characteristics of the fresh device and the degraded device after 1,000 h stress application at P3. The leakage currents observed for the fresh device due to packaging [Jac15] have no impact in the degradation analysis and are not taken into account. Since the recombination process has no considerable impact on the collector current, the resulting increase in the base current degrades the current gain of the transistor.

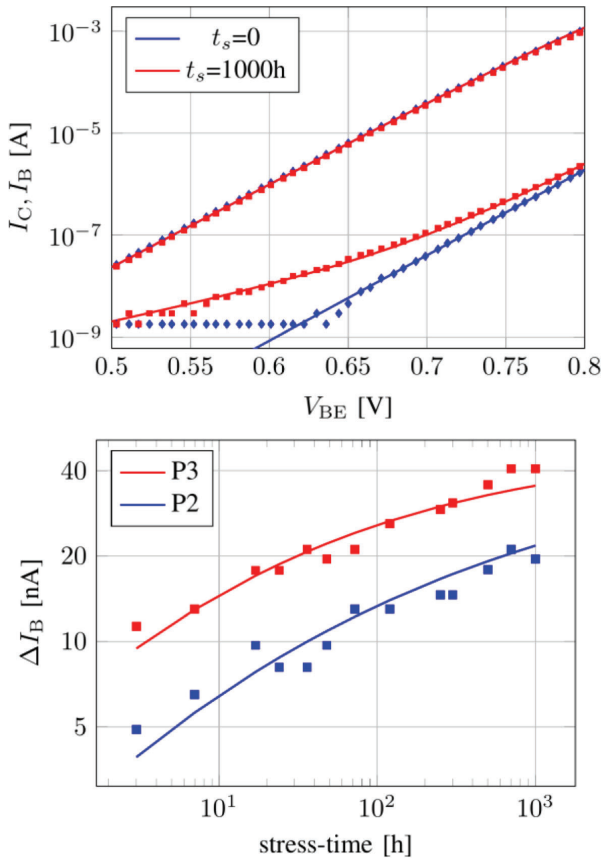

Figure 2.40 (Top) Gummel characteristics (V_{CB} = 0 V) of the fresh and degraded SiGe HBT after 1,000 h at P3 obtained from simulation (lines) and measurement (symbols). (Bottom) Excess base currents over the stress time obtained from simulation (lines) and measurement (symbols) at V_{BE} = 0.67 V and V_{CB} = 0 V.

In order to assess the time dependence of the HCD effects, the excess base current $\Delta I_{\mathrm{B}} = I_{\mathrm{B}}(t) - I_{\mathrm{B}}(0)$ is extracted over stress time [Figure 2.14 (bottom)]. Very good agreement between the simulation results and measurement data proves that the EDF-based degradation model can directly explain the time dynamics of the HCD results together with their dependence on the stress bias conditions.

References

[Bea92] J. C. Bean. Silicon-based semiconductor heterostructures: column IV bandgap engineering. Proceedings of IEEE, pp. 571–589, April 1992.

[Bin14] Bina, M., et al. (2014). Predictive hot-carrier modeling of n-channel MOSFETs. *IEEE Trans. Electron Devices* 61, 3103–3110.

[Blo70] K. Blotekjaer, Transport equations for electrons in two-valley semiconductors. *IEEE Transactions on Electron Devices*, vol. ED-17, no. 1, pp. 38–47, 1970.

[Che07] Cheng, P., et al. (2007). Understanding radiation-and hot carrier-induced damage processes in SiGe HBTs using mixed-mode electrical stress. *IEEE Trans. Nucleic Sci.* 54, 1938–1945.

[Che09] Cheng, P., Grens, C. M., and Cressler, J. D. (2009). Reliability of SiGe HBTs for power amplifiers-Part II: Underlying physics and damage modeling. *IEEE Trans. Electron Devices* 9, 440–448.

[Cre04] Cressler, J. D. (2004). Emerging SiGe HBT reliability issues for mixed-signal circuit applications. *IEEE Trans. Device Mater. Reliab.* 4, 222–236.

[d'Al02] d'Alessandro, V., and Rinaldi, N. (2002). A critical review of thermal models for electro-thermal simulation. *Solid State Electron.* 46, 487–496.

[d'Al14] d'Alessandro, V., Sasso, G., Rinaldi, N., and Aufinger, K. (2014). Influence of scaling and emitter layout on the thermal behavior of toward-THz SiGe: C HBTs. *IEEE Trans. Electron Devices* 61, 3386–3394.

[d'Al16] d'Alessandro, V., Magnani, A., Codecasa, L., Rinaldi, N., and Aufinger, K. (2016). Advanced thermal simulation of SiGe:C HBTs including back-end-of-line. *Microelectron. Reliab.* 67, 38–45.

[DiM01] D. J. DiMaria and J. H. Stathis, Anode hole injection, defect generation, and breakdown in ultrathin silicon dioxide films. *J. Appl. Phys.*, vol. 89, no. 9, pp. 5015–5024, May 2001.

[DiM89] DiMaria, D. J., and Stasiak, J. W. (1989). Trap creation in silicon dioxide produced by hot electrons. *J. Appl. Phys.*, vol. 65, no. 6, pp. 2342–2356, Mar. 1989.

[Fis15] G. G. Fischer and G. Sasso, Ageing and thermal recovery of advanced SiGe heterojunction bipolar transistors under long-term mixed-mode and reverse stress conditions. *Microelectron. Reliab.*, vol. 55, no. 3, pp. 498–507, Mar. 2015.

[Gal05] M. Galler. Mulitgroup Equations for the Description of the Particle Transport in Semiconductors, Vol. 70, World Scientific, 2005.

[Gnu93] A. Gnudi, D. Ventura, G. Baccarani, and F. Odeh, Two-dimensional MOSFET simulation by means of a multidimensional spherical harmonics expansion of the Boltzmann transport equation. *Solid State Electron.*, vol. 36, no. 4, pp. 575 – 581, Apr. 1993.

[Gra14] T. Grasser, K. Rott, H. Reisinger, M. Waltl, F. Schanovsky, and B. Kaczer, NBTI in nanoscale MOSFETs-the ultimate modeling benchmark. *IEEE Trans. Electron Devices*, vol. 61, no. 11, pp. 3586–3593, Nov. 2014.

[Her56] C. Herring and E. Vogt. Transport and deformation – potential theory for many – valley semiconductors with anisotropic scattering. *Physical Review*, Vol. 101, pp. 944–961, Feb. 1956.

[Hon11] S.-M. Hong, A.-T. Pham, and C. Jungemann. *Deterministic Solvers for the Boltzmann Transport Equation*, Springer, 2011.

[Hur92] G. Hurkx, D. Klaassen, and M. Knuvers, A new recombination model for device simulation including tunneling. *IEEE Trans. Electron Devices*, vol. 39, no. 2, pp. 331–338, Feb. 1992.

[Jab14] D. Jabs and C. Jungemann, "Avalanche breakdown of pn-junctions-Simulation by spherical harmonics expansion of the Boltzmann transport equation," in *Proc. Int. Conf. Simulation Semiconductor Process. Devices (SISPAD)*, Sep. 2014, pp. 173–176.

[Jac15] T. Jacquet *et al.*, Reliability of high-speed SiGe: C HBT under electrical stress close to the SOA limit. *Microelectron. Reliab.*, vol. 55, no. 9, pp. 1433–1437, Sep. 2015.

[Jac83] C. Jacoboni and L. Reggiani. The Monte Carlo method for the solution of charge transport in semiconductors with applications to covalent materials. *Reviews of Modern Physics*, vol. 55, pp. 645–705, July 1983.

[Jep77] K. O. Jeppson and C. M. Svensson, Negative bias stress of MOS devices at high electric fields and degradation of MNOS devices. *J. Appl. Phys.*, vol. 48, no. 5, pp. 2004–2014, May 1977.

[Jun03]C. Jungemann and B. Meinerzhagen. Hierarchical Device Simulation – The Monte-Carlo Perspective. Springer, 2003.

[Jun07] C. Jungemann, "A deterministic solver for the Langevin Boltzmann equation including the Pauli principle," *Proc. SPIE, Noise and Fluctuations in Circuits, Devices, and Materials*, vol. 6600, no. 1, p. 660007, May 2007.

[Kam15] H. Kamrani, T. Kochubey, D. Jabs, and C. Jungemann, "Electrothermal simulation of SiGe HBTs and investigation of experimental extraction methods for junction temperature," in *Proc. IEEE Int. Conf. Simulation Semiconductor Process. Devices (SISPAD)*, Sep. 2015, pp. 108–111.

[Kam16] H. Kamrani, D. Jabs, V. d'Alessandro, N. Rinaldi, and C. Jungemann, "Physics-based hot-carrier degradation model for SiGe HBTs," in *Proc. Int. Conf. Simulation Semiconductor Process. Devices (SISPAD)*, 2016, pp. 341–344.

[Kam17a] H. Kamrani, D. Jabs, V. d'Alessandro, N. Rinaldi, K. Aufinger, and C. Jungemann, "A deterministic and self-consistent solver for the coupled carrier-phonon system in SiGe HBTs," accepted in *IEEE Trans. Electron Devices*.

[Kam17b] H. Kamrani, *et al.*, "Microscopic hot-carrier degradation modeling of SiGe HBTs under stress conditions close to the SOA limit," submitted in *IEEE Trans. Electron Devices*.

[Kor15] J. Korn, H. Ruecker, B. Heinemann, A. Pawlak, G. Wedel, and M. Schroter. Experimental and Theoretical Study of fT for SiGe HBTs with a Scaled Vertical Doping Profile, Proc. IEEE BCTM, Boston, pp. 117–120, 2015.

[Kuf07] H. Kufluoglu and M. A. Alam, "A generalized reaction-diffusion model with explicit H-H2 dynamics for negative-bias temperature-instability (NBTI) degradation," *IEEE Trans. Electron Devices*, vol. 54, no. 5, pp. 1101–1107, 2007.

[Lee12] Y. Lee and G. S. Hwang, "Mechanism of thermal conductivity suppression in doped silicon studied with nonequilibrium molecular dynamics," *Phys. Rev. B*, vol. 86, no. 7, pp. 075 202-1–075 202-6, Aug. 2012.

[Lun00] M. Lundstrom. *Fundamentals of Carrier Transport*. Cambridge University Press, 2000.

[Mar09] I. Marano, V. d'Alessandro, and N. Rinaldi, "Analytical modeling and numerical simulations of the thermal behavior of trench-isolated

bipolar transistors," *Solid State Electron.*, vol. 53, no. 3, pp. 297–307, Mar. 2009.

[Moe12] K. A. Moen, P. S. Chakraborty, U. S. Raghunathan, J. D. Cressler, and H. Yasuda, "Predictive physics-based TCAD modeling of the mixed-mode degradation mechanism in SiGe HBTs," *IEEE Trans. Electron Devices*, vol. 59, no. 11, pp. 2895–2901, Nov. 2012.

[Mus08] O . Muscato, V. Di Stefano, and C. Milazzo, "An improved hydrodynamic model describing heat generation and transport in submicron silicon devices," *J. Comput. Electron.*, vol. 7, no. 3, pp. 142–145, Sep. 2008.

[Ngh14] T. Thu Trang Nghiem, J. Saint-Martin, and P. Dollfus, "New insights into self-heating in double-gate transistors by solving boltzmann transport equations," *J. Appl. Phys.*, vol. 116, no. 7, pp. 074 514-1–074 514-9, Aug. 2014.

[Ni12] C. Ni, Z. Aksamija, J. Y. Murthy, and U. Ravaioli, "Coupled electrothermal simulation of MOSFETs," *J. Comput. Electron.*, vol. 11, no. 1, pp. 93–105, Mar. 2012.

[Pal04] V. Palankovski and R. Quay, *Analysis and simulation of heterostructure devices*. Vienna, Austria: Springer-Verlag, 2004.

[Paw09] A. Pawlak, M. Schröter, J. Krause, G. Wedel, and C. Jungemann. On the Feasibility of 500 GHz Silicon-Germanium HBTs, SISPAD 2009, San Diego, CA, 2009, pp. 1–4.

[Paw17] A. Pawlak, B. Heinemann, and M. Schröter, "Physics-based modeling of SiGe HBTs with f_{T} of 450 GHz with HICUM Level 2", IEEE BCTM, Miami , FL, p. 4, 2017.

[Pob13] G. Pobegen, S. Tyaginov, M. Nelhiebel, and T. Grasser, "Observation of normally distributed energies for interface trap recovery after hot-carrier degradation," *IEEE Electron Device Lett.*, vol. 34, no. 8, pp. 939–941, Aug. 2013.

[Pop05] E. Pop, R. W. Dutton, and K. E. Goodson, "Monte Carlo simulation of Joule heating in bulk and strained silicon," *Appl. Phys. Lett.*, vol. 86, no. 8, pp. 082 101-1–082 101-3, Feb. 2005.

[Pop06] E. Pop, S. Sinha, and K. E. Goodson, "Heat generation and transport in nanometer-scale transistors," *Proc. IEEE*, vol. 94, no. 8, pp. 1587–1601, Aug. 2006.

[Pop10] E. Pop, "Energy dissipation and transport in nanoscale devices," *Nano Research*, vol. 3, no. 3, pp. 147–169, Mar. 2010.

[Rag15] U. S. Raghunathan *et al.*, "Bias-and temperature-dependent accumulated stress modeling of mixed-mode damage in SiGe HBTs," *IEEE Trans. Electron Devices*, vol. 62, no. 7, pp. 2084–2091, Jul. 2015.

[Ral08] K. Raleva, D. Vasileska, S. M. Goodnick, and M. Nedjalkov, "Modeling thermal effects in nanodevices," *IEEE Trans. Electron Devices*, vol. 55, no. 6, pp. 1306–1316, Jun. 2008.

[Ram15] M. Ramonas and C. Jungemann, "A deterministic approach to noise in a non-equilibrium electron-phonon system based on the Boltzmann equation," *J. Comput. Electron.*, vol. 14, no. 1, pp. 43–50, Mar. 2015.

[Rup16] K. Rupp, C. Jungemann, S. M. Hong, M. Bina, T. Grasser, and A. Jungel, "A review of recent advances in the spherical harmonics expansion method for semiconductor device simulation," *J. Comput. electron.*, pp. 1–20, May 2016.

[Sad10] T. Sadi and R. W. Kelsall, "Monte Carlo study of the electrothermal phenomenon in silicon-on-insulator and silicon-germanium-on-insulator metal-oxide field-effect transistors," *J. Appl. Phys.*, vol. 107, no. 6, pp. 064 506-1–064 506-9, Mar. 2010.

[Sch06] M. Schröter, H. Tran. Charge-storage related parameter calculations for Si and SiGe bipolar transistors from device simulation, Proc. WCM, International NanoTech Meeting, Boston , MA, pp. 735–740, 2006.

[Sch11] M. Schröter, G.Wedel, B. Heinemann, C. Jungemnn, J. Krause, P. Chevalier, and A. Chantre. Physical and Electrical Performance Limits of High-Speed SiGeC HBTs-Part I: Vertical Scaling, IEEE Transactions on Electron Devices, Vol. 58, No. 11, pp. 3687–3696, Nov. 2011.

[Sch17] M. Schröter, T. Rosenbaum, P. Chevalier, B. Heinemann, S. Voinigescu, E. Preisler, J.Boeck, and A. Mukherjee. SiGe HBT technology: Future trends and TCAD based roadmap, Proc. of the IEEE, Vol. 105, No. 6, pp. 1068–1086, 2017.

[Sel84] S. Selberherr. Analysis and Simulation of Semiconductor Devices. Springer, 1984.

[Sha15] P. Sharma *et al.*, "Modeling of hot-carrier degradation in nLDMOS devices: different approaches to the solution of the Boltzmann transport equation," *IEEE Trans. Electron Devices*, vol. 62, no. 6, pp. 1811–1818, Jun. 2015.

[Slo77] J. W. Slotboom and H. C. de Graaff. Bandgap narrowing in silicon bipolar transistors. *IEEE Trans. Electron Devices*, vol. 24, no. 8, pp. 1123–1125, Aug. 1977.

[Sta11] I. Starkov *et al.*, "Hot-carrier degradation caused interface state profile- simulation versus experiment," *J. Vac. Sci. Technol. B*, vol. 29, no. 1, pp. 01AB091–01AB098, Jan. 2011.

[Sta12] I. Starkov, H. Enichlmair, S. Tyaginov, and T. Grasser, "Charge-pumping extraction techniques for hot-carrier induced interface and oxide trap spatial distributions in MOSFETs," in *Physical and Failure Analysis of Integrated Circuits (IPFA)*, July 2012, pp. 1–6.

[Ste96] A. Stesmans, "Revision of H2 passivation of pb interface defects in standard (111) Si/SiO2," *Appl. Phys. Lett.*, vol. 68, no. 19, pp. 2723–2725, Feb. 1996.

[Sto98] K. Stokbro *et al.*, "STM-induced hydrogen desorption via a hole resonance," *Phys. Rev. Lett.*, vol. 80, no. 12, pp. 2618–2621, Mar. 1998.

[Str62] R. Stratton. Diffusion of hot and cold electrons in semiconductor barriers. Physical Review, vol. 126, no. 6, pp. 2002–2014, 1962.

[Syn15] Synopsys, Inc., 690 E. Middlefield Road Mountain View, CA 94041. Sentaurus Device User Guide, version k-2015.06 edition, June 2015.

[Tom93] K. Tomizawa. Numerical Simulation of Submicron Semiconductor Devices. Artech House Boston, London, 1993.

[Tya16] S. Tyaginov, M. Jech, J. Franco, P. Sharma, B. Kaczer, and T. Grasser, "Understanding and modeling the temperature behavior of hot-carrier degradation in SiON n-MOSFETs," *IEEE Electron Device Lett.*, vol. 37, no. 1, pp. 84–87, Jan. 2016.

[Van] T. Vanhoucke *et al.*, "Physical description of the mixed-mode degradation mechanism for high performance bipolar transistors," in *Proc. IEEE Bipolar/BiCMOS Circuits Technol. Meeting*, 2006, pp. 25–28.

[Vas09] D. Vasileska, K. Raleva, and S. M. Goodnick, "Self-heating effects in nanoscale FD SOI devices: the role of the substrate, boundary conditions at various interfaces, and the dielectric material type for the box," *IEEE Trans. Electron Devices*, vol. 56, no. 12, pp. 3064–3071, Dec. 2009.

[Vas10] D. Vasileska, K. Raleva, and S. M. Goodnick, "Electrothermal studies of FD SOI devices that utilize a new theoretical model for the temperature and thickness dependence of the thermal conductivity," *IEEE Trans. Electron Devices*, vol. 57, no. 3, pp. 726–728, Mar. 2010.

[Wed10] G. Wedel and M. Schröter. Hydrodynamic simulations for advanced SiGe HBTs. IEEE Bipolar/BiCMOS Circuits and Technology Meeting (BCTM) 2010, pp. 237–244, Oct 2010.

[Wed16] G. Wedel. A Box-Integration/WENO solver for the Boltzmann Transport Equation and its Application to High-Speed Heterojunction Bipolar Transistors. PhD thesis, Technische Universitt Dresden, 2016.

[Wie16] B. R. Wier, K. Green, J. Kim, D. T. Zweidinger, and J. D. Cressler, "A physics-based circuit aging model for mixed-mode degradation in SiGe HBTs," *IEEE Trans. Electron Devices*, vol. 63, no. 8, pp. 2987–2993, Aug. 2016.

[Zeb06] M. Zebarjadi, A. Shakouri, and K. Esfarjani, "Thermoelectric transport perpendicular to thin-film heterostructures calculated using the Monte Carlo technique," *Phys. Rev. B*, vol. 74, no. 19, pp. 195 331-1–195 331-6, Nov. 2006.